
Masters Theses

Student Theses and Dissertations

Fall 2015

Emission source microscopy applications on EMI source localization and EMI mitigation with lossy materials

Xiangyang Jiao

Follow this and additional works at: https://scholarsmine.mst.edu/masters_theses



Part of the [Electromagnetics and Photonics Commons](#)

Department:

Recommended Citation

Jiao, Xiangyang, "Emission source microscopy applications on EMI source localization and EMI mitigation with lossy materials" (2015). *Masters Theses*. 7467.

https://scholarsmine.mst.edu/masters_theses/7467

This thesis is brought to you by Scholars' Mine, a service of the Missouri S&T Library and Learning Resources. This work is protected by U. S. Copyright Law. Unauthorized use including reproduction for redistribution requires the permission of the copyright holder. For more information, please contact scholarsmine@mst.edu.

EMISSION SOURCE MICROSCOPY APPLICATIONS ON EMI SOURCE
LOCALIZATION AND EMI MITIGATION WITH LOSSY MATERIALS

by

XIANGYANG JIAO

A THESIS

Presented to the Faculty of the Graduate School of the
MISSOURI UNIVERSITY OF SCIENCE AND TECHNOLOGY

In Partial Fulfillment of the Requirements for the Degree

Master of SCIENCE

in

ELECTRIC ENGINEERING

2015

Approved
Dr. David Pommerenke, Advisor
Dr. Jun Fan
Dr. Yahong Rosa Zheng

© 2015

XIANGYANG JIAO

All Rights Reserved

ABSTRACT

In Section 1, the emission source microscopy (ESM) methodology will be introduced and used to identify the sources of radiation on different DUTs. As the new technology generation, the integration density and the operating speed of integrated circuits have been increasing steadily. However, root cause diagnostics to locate the source of EMI radiation is more problematic in the complex system. The ESM technique provides a powerful tool to detect and characterize the active sources of radiation. The amplitude and phase of fields are measured on a plane away from the DUT, and this measurement can get rid of the evanescent waves influence in the near field. The ESM algorithm is then applied to propagate the fields back to the source plane and to localize the sources of radiation. The ESM method is used on different DUTs at different frequencies to evaluate the source identification performance. The results show that the proposed method is capable of detecting multiple active sources on a complex system.

In section 2, the possibility of building channel emulators by utilizing fused deposition modeling (FDM) 3D printing technology is investigated. The FDM 3D printing provides a rapid and economic method to produce parts with different shapes. An optimizing algorithm was developed for obtaining the printing pattern and loss profile. Those parts with different dielectric constants and loss tangents will be printed on a low loss transmission line to modify its transmission or reflection. As a result, different channel emulators can be built to emulate the S-parameter and eye diagrams of a target channel with the advantage of avoiding complicated electronic components.

ACKNOWLEDGMENTS

I would like to express my sincere gratitude to my advisor Prof. David Pommerenke and my co-advisor Prof. James Drewniak for their guidance throughout my master study. Dr. Pommerenke gives me the most helpful instruction and the guidance for my study and research. His passions on the EMC area enlighten my research motion and inspire me continue on this road. Dr. James Drewniak is my mentor on my study and life. I would sincerely thanks for his trust and encouragement when I came into the lab. His talk and guidance shaped me as a responsible and mature person.

I would like to specially thank Dr. Daryl Beetner, Dr. Jun Fan and Dr. Victor Khilkevich for their valuable advice and support during my study in the EMC lab. And I would like to thank Dr. Rosa Zheng for her advice and support on my dissertation.

I would like to express my thanks to all of other faculty members and my fellow lab mates in the EMC group of Missouri S&T for their great team work and help in my research and coursework. There are cheerful and miserable experiences during my study, but for all of these memories I will never forget.

I would also like to thanks the teams from Cisco and Laird Company. It is really a great honor to be able to work with the team and thanks for their useful guidance and advise for my research.

Finally, I am deeply grateful to my family to their constant support. Especially, I would like to express my love for my wife Qian. We walked through our most difficult time together and she always supports me in my life and study. I would like to thanks for her love, trust and support to me during our study time.

TABLE OF CONTENTS

	Page
ABSTRACT	iii
ACKNOWLEDGMENTS	iv
LIST OF ILLUSTRATIONS	vii
LIST OF TABLES	ix
SECTION	
1. EMISSION SOURCE MICROSCOPY APPLICATIONS ON EMI SOURCE LOCALIZATION AND EMI MITIGATION WITH LOSSY MATERIALS	1
1.1. INTRODUCTION	1
1.2. EMISSION SOURCE MICROSCOPY METHODOLOGY	2
1.2.1. Wave Diffraction and Fourier Transform	3
1.2.2. Angular Spectrum Method	6
1.2.3. Resolution of Diffraction-Limited System.....	9
1.3. CASE 1: SOURCE IDENTIFICATION ON NETWORK SWITCH	11
1.3.1. ESM Measurement Setup.....	11
1.3.2. Source Identification with ESM Method.....	13
1.3.3. EMI Mitigation with Lossy Material.....	17
1.3.4. Total Radiated Power Comparison.....	19
1.3.5. Conclusion.....	20
1.4. CASE 2: SOURCE IDENTIFICATION ON COMPUTER SCREEN	20
1.4.1. Introduction of the Flex Printed Circuit	21
1.4.2. ESM Measurement Setup with Manually Scanning System.....	22
1.4.3. ESM for the Source Identification and EMI Mitigation with Absorber.....	23
1.4.4. Far Field Measurement of the Computer Screen in the 3 m Chamber...	27
1.4.5. Conclusion.....	29
1.5. CASE 3: RADIATION FROM HEATSINKS AND MITIGATION USING ABSORBING MATERIALS	29
1.5.1. Introduction of the Heatsink Radiation	29
1.5.2. Heatsink Modeling and the S-parameters Comparison	30
1.5.3. Heatsink Total Radiation Measurement	33

1.5.4. Near Field to Far Field Transformation	36
1.5.5. Conclusion.....	40
1.6. CONCLUSION & FUTURE WORK.....	41
2. DESIGNING A 3D PRINTING-BASED CHANNEL EMULATOR WITH PRINTABLE ELECTROMAGNETIC MATERIALS.....	43
2.1. ABSTRACT.....	43
2.2. INTRODUCTION	43
2.3. LOW LOSS TRANSMISSION LINE DESIGN	45
2.4. DEVELOPMENT OF 3D PRINTING FILAMENT WITH HIGH DIELECTRIC CONSTANTS AND LOSS PROPERTY	46
2.4.1. Printable High Dielectric Constant Materials	47
2.4.2. Printable Electrically Lossy Materials	51
2.4.3. Printable Magnetically Lossy Materials.....	54
2.5. DETERMINE 3D PRINTING PROFILE FOR A CHANNEL EMULATOR.	57
2.6. TEST CASES	60
2.7. CONCLUSIONS	64
BIBLIOGRAPHY.....	65
VITA	71

LIST OF ILLUSTRATIONS

	Page
Figure 1.1. Geometry of diffraction theory.....	4
Figure 1.2. Propagation of a plane-wave component in the angular spectrum.....	7
Figure 1.3. Aperture angle of the scanning system.....	10
Figure 1.4. Radiation spectrum from the DUT.....	12
Figure 1.5. ESM test setup for the real hardware measurement.....	12
Figure 1.6. The schematic diagram of the ESM measurement setup.....	13
Figure 1.7. Measured E field distribution at the scanning plane.....	15
Figure 1.8. Measured total tangential field component with near field scanning.....	16
Figure 1.9. Reconstructed E_x and E_y field component at the PCB plane.....	18
Figure 1.10. 4 pieces of absorbers applied on the source location.....	18
Figure 1.11. Reconstructed E_x and E_y fields at the PCB plane.....	18
Figure 1.12. Setup for the TRP measurement in a reverberation chamber.....	19
Figure 1.13. TRP spectrums comparison with and without the absorber material.....	20
Figure 1.14. Back side of the computer screen.....	21
Figure 1.15. Sketch diagram of the Emission Source Microscopy technology.....	22
Figure 1.16. ESM setup on the computer screen.....	23
Figure 1.17. Back side of the computer screen.....	23
Figure 1.18. Scanning plane magnitude and the phase distribution.....	24
Figure 1.19. Focusing plane field distribution.....	24
Figure 1.20. Reduce the distance between the antenna and the DUT to 25 cm.....	25
Figure 1.21. Focusing plane field distribution with different scanning heights.....	25
Figure 1.22. Field comparison with and without absorber applied.....	26
Figure 1.23. Far Field measurement of the computer screen in the 3 m chamber.....	28
Figure 1.24. Far Field comparison with and without absorber.....	28
Figure 1.25. The simulation model and experiment measurement setup of the heatsink.	31
Figure 1.26. The simulated and measured S_{11} parameter of the heatsink with and without the absorbing materials.....	32
Figure 1.27. The simulated and measured S_{21} parameter of the heatsink with and without the absorbing materials.....	32
Figure 1.28. Feature selection validation results with global difference measure confidence histograms for heatsink application.....	33
Figure 1.29. Setup for the chamber calibration.....	34

Figure 1.30. Setup for the total radiated power measurement of the heatsink.....	35
Figure 1.31. Comparison of simulated and measured results of radiation power.....	36
Figure 1.32. Comparison of simulated and measured results of total radiation reduction	36
Figure 1.33. Near field scanning setup for the heatsink radiation	37
Figure 1.34. E field probe used for the near field scanning setup	38
Figure 1.35. The CST model of the heatsink	38
Figure 1.36. E field probe used for the near field scanning setup	39
Figure 1.37. Comparison of the total radiated power results with different methodologies.....	40
Figure 2.1. Full-wave CST model and pictures of low loss microstrip trace..	45
Figure 2.2. Comparison of measured and simulated transmission coefficients S_{21} of the low loss microstrip trace.....	46
Figure 2.3. Printed blocks with different mixing ratios of TiO_2 and different sizes.....	49
Figure 2.4. The real part and imaginary part of measured permittivity of different TiO_2 ratio mixed high permittivity materials.	50
Figure 2.5. Comparison of S_{21} parameters with different lengths of carbomorph blocks placed on the trace.....	52
Figure 2.6. The comparison of measured Carbonara material parameters with the CST setting	53
Figure 2.7. Measured and simulated S_{21} parameters comparison using a 1 cm by 1 cm by 0.2 cm carbonara block on the trace	54
Figure 2.8. The measured complex permittivity and permeability of two magnetically lossy materials with 30% and 85% CI weight ratios	55
Figure 2.9. Attenuation coefficient α comparison of raw magnetically lossy material with different CI weight ratios	56
Figure 2.10. Comparison of the attenuation coefficients of electrically and magnetically lossy materials.....	57
Figure 2.11. A typical S_{21} parameter target function from 100 kHz to 8.5 GHz	57
Figure 2.12. Flow chart for determining the printing profile for the channel emulator ...	58
Figure 2.13. Printing pattern on the simulated channel	60
Figure 2.14. S_{21} comparison of the target channel, simulation and measurement results.	61
Figure 2.15. Printing high dielectric constant material blocks on the trace.....	62
Figure 2.16. Comparison of eye diagrams from the target and the emulated channel.. ...	63

LIST OF TABLES

	Page
Table 1.1. Spread – Grade data for the heatsink application example for Global Difference Measure.	33
Table 2.1 Optimized printer settings for the different materials.....	47
Table 2.2 Material density comparison.....	48
Table 2.3 Eye diagram parameters comparison.....	64

1. EMISSION SOURCE MICROSCOPY APPLICATIONS ON EMI SOURCE LOCALIZATION AND EMI MITIGATION WITH LOSSY MATERIALS

1.1. INTRODUCTION

As the new technology generation, the integration density and the operating speed of integrated circuits have been increasing steadily. However, root cause diagnostics to locate the source of EMI radiation is more problematic in the complex system. In general, near-field scanning methodology is often used to locate the source of EMI radiation [1]. This method can provide us the radiated and reactive near field distribution on the device under test (DUT). However, in practice the near-field technique has difficulties in placing the probe close enough to the complex and sensitive DUT. Furthermore, EMC engineers are primarily concerned with the sources of EMI contributing to far-field radiation only, which near field scanning is often not capable of identifying the causes of EMI radiation [1]. The emission source microscopy (ESM) technique provides a powerful tool to detect and characterize the active sources of radiation in a complex system. In the ESM method, the amplitude and phase of fields are measured on a plane away from the DUT. The ESM algorithm is then applied to propagate the fields back to the source plane and to localize the sources of radiation [2].

Absorbing materials for reduction of electromagnetic interference (EMI) are typically used at later stages of electronic product development as a practical countermeasure to possible regulatory issues. However, design consideration for absorbing materials at earlier stages could be beneficial to provide cost-effective solutions. These include cavity/chassis resonances suppression, common mode current suppression on attached harness/wire structures, heatsink radiation mitigation, intrasystem interference between different modules of a product, and many more [2]-[6].

However, some questions arise when absorbing materials need to be applied.

Which material should be selected? Where should it be applied? How much is needed?

The ESM methodology provides a powerful tool for locating the sources of radiation in GHz range within the complex system. Once the source is identified, a suitable volume of the absorber material can be placed on the source location to effectively reduce the radiated power at the frequency of interest. By placing the lossy material on the source location it can effectively reduce the radiation over a broadband frequency range, without requiring additional design changes to the DUT.

1.2. EMISSION SOURCE MICROSCOPY METHODOLOGY

In literature, synthetic aperture radar (SAR) techniques are mainly used for antenna diagnostics and antenna pattern measurement [7]. Such techniques also have been used for microwave imaging to detect concealed objects and structural defects [8]-[12]. Standard SAR methods use signals reflected from the target and received by a scanning antenna to reconstruct the target's image. Based on the SAR technique, the ESM algorithm is used to identify sources of radiation on a complex system. The scanning hardware is used to move the antenna on the scanning plane and it collects fields over a synthetic aperture. Both of the amplitude and phase information of the field in the scanning plane must be collected. The fields can be translated by transforming the fields from the spatial to the spatial frequency domain. Then they can be back propagated to the source plane. On the source plane, they are back converted to spatial domain to retrieve the focused image. The focused image on the source plane provides the information about the sources of radiation.

1.2.1. Wave Diffraction and Fourier Transform. Wave diffraction and Fourier transform are the foundations of the theory of emission source microscopy technology. The theory of propagation and diffraction of electromagnetic fields has a long history of development and has many subtleties that need to be considered carefully in order to arrive at accurate and consistent results [13]. In 1678, Huygens proposed that every point which a luminous disturbance reaches becomes a source of a spherical wave; the sum of these secondary waves determines the form of the wave at any subsequent time [14]. Base on this theory, the geometry which shows in Fig. 1.1 is considered. The input field $E_0(x_0, y_0, 0)$ on the input plane Σ_0 propagates along the z -direction and results in the output field $E_z(x, y, z)$ on the output plane Σ . Then electrical field on the output z plane is written as [15]

$$\begin{aligned}
 E_z(x, y, z) &= -\frac{ik}{2\pi} \iint_{\Sigma_0} dx_0 dy_0 E_0(x_0, y_0, 0) \frac{\exp(ikr)}{r} \\
 &\approx -\frac{ik}{2\pi z} \iint_{\Sigma_0} dx_0 dy_0 E_0(x_0, y_0, 0) \exp\left[ik\sqrt{(x-x_0)^2 + (y-y_0)^2 + z^2} \right]
 \end{aligned}
 \tag{1.1}$$

where $k = 2\pi/\lambda$ is the free space wavenumber. An approximation of $r \approx z$ in the denominator was made, but not in the exponent.

Fresnel diffraction: The Fresnel diffraction equation for near-field diffraction is an approximation of Kirchhoff-Fresnel diffraction that can be applied to the propagation of waves in the near field [17]. It is used to calculate the diffraction pattern created by waves passing through an aperture or around an object, when viewed from relatively close to the object. For theoretical developments and other purposes, it is often useful to make paraxial, or Fresnel, approximation [15]

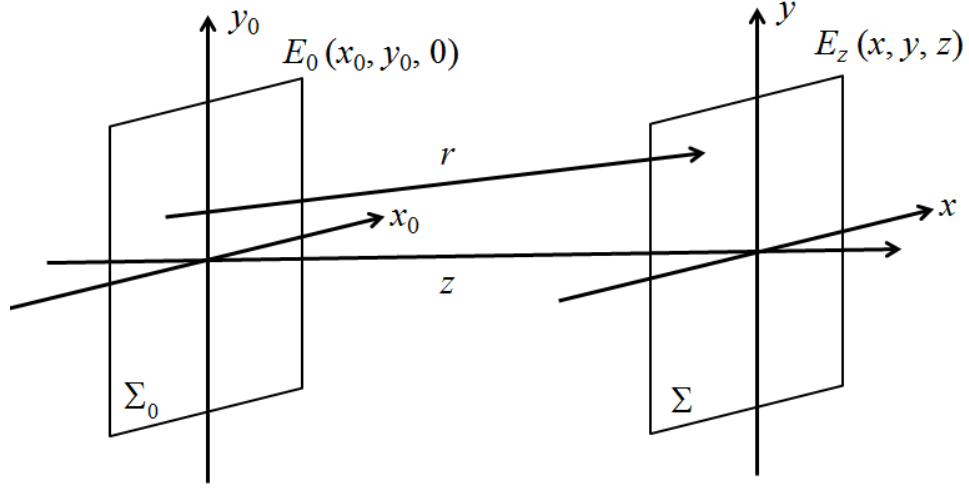


Figure 1.1. Geometry of diffraction theory.

$$r = \sqrt{(x-x_0)^2 + (y-y_0)^2 + z^2} \approx z + \frac{(x-x_0)^2 + (y-y_0)^2}{2z} \quad (1.2)$$

which is valid for $z^3 \gg \frac{k}{8} [(x-x_0)^2 + (y-y_0)^2]_{\max}^2$. Then electrical field on the

output z plane is written as

$$\begin{aligned} E_z(x, y, z) &= -\frac{ik}{2\pi z} \iint_{\Sigma_0} dx_0 dy_0 E_0(x_0, y_0, 0) \exp\left[ik\sqrt{(x-x_0)^2 + (y-y_0)^2 + z^2}\right] \\ &\approx -\frac{ik}{2\pi z} \exp(ikz) \iint_{\Sigma_0} dx_0 dy_0 E_0(x_0, y_0, 0) \exp\left\{\frac{ik}{2z} [(x-x_0)^2 + (y-y_0)^2]\right\} \\ &= -\frac{ik}{2\pi z} \exp(ikz) \exp\left[\frac{ik}{2z}(x^2 + y^2)\right] \times \iint_{\Sigma_0} dx_0 dy_0 E_0(x_0, y_0, 0) \exp\left[\frac{ik}{2z}(x_0^2 + y_0^2)\right] \exp\left[\frac{ik}{z}(xx_0 + yy_0)\right] \\ &= -\frac{ik}{z} \exp(ikz) \exp\left[\frac{ik}{2z}(x^2 + y^2)\right] \mathbf{F}\left\{E_0(x_0, y_0, 0) \exp\left[\frac{ik}{2z}(x_0^2 + y_0^2)\right]\right\} \end{aligned} \quad (1.3)$$

\mathbf{F} is the forward Fourier transform operator. Equation 1.3 is referred to as the Fresnel transform. In the Fresnel approximation, the electrical field on the output plane is proportional to the Fourier transform of the input field multiplied by a secondary phase

factor $\exp[ik(x_0^2+y_0^2)/2z]$. From Equation 1.3, it can be seen that the secondary phase factor $\exp[ik(x^2+y^2)/2z]$, which is outside of the Fourier transform, does not influence the electrical field distribution on the output plane. However, the secondary phase factor $\exp[ik(x_0^2+y_0^2)/2z]$, which is inside of the Fourier transform, has a strong influence on the intensity distribution of output field. The electrical field distribution on the output plane will depend on the distance z between the input plane and output plane. When the distance z is large enough, the influence of the secondary phase factor $\exp[ik(x_0^2+y_0^2)/2z]$ will be neglected. This will lead over to another diffraction theory: Fraunhofer diffraction.

Fraunhofer diffraction: The Fraunhofer diffraction equation is used to model the diffraction of waves when the diffraction pattern is viewed at a long distance from the diffracting object, and also when it is viewed at the focal plane of an imaging lens [18]. In the Fresnel approximation, if using one further approximation and ignore terms of the

order $\frac{x_0^2 + y_0^2}{z^2} \ll 1$ to write

$$r = \sqrt{(x-x_0)^2 + (y-y_0)^2 + z^2} \approx z + \frac{x^2 + y^2}{2z} - \frac{xx_0 + yy_0}{z} \quad (1.4)$$

then electrical field on the output z plane is written as [15]

$$\begin{aligned} E_z(x, y, z) &\approx -\frac{ik}{2\pi z} \exp(ikz) \exp\left[\frac{ik}{2z}(x^2 + y^2)\right] \times \iint_{\Sigma_0} dx_0 dy_0 E_0(x_0, y_0, 0) \exp\left[\frac{ik}{2z}(xx_0 + yy_0)\right] \\ &= -\frac{ik}{z} \exp(ikz) \exp\left[\frac{ik}{2z}(x^2 + y^2)\right] \mathbf{F}\{E_0(x_0, y_0, 0)\} \end{aligned} \quad (1.5)$$

The output field is proportional to the Fourier transform of the input field. It means the Fraunhofer diffraction in this system is also the Fourier transform of the input field in the system. The diffracted field distribution is the spatial-frequency distribution of the input

field. Therefore, for example, the Fraunhofer diffraction pattern of a rectangular aperture is a sinc function and for a circular aperture it is an Airy disk pattern.

1.2.2. Angular Spectrum Method. In last section, it is found that it is convenient to regard each point on the aperture as a new source of spherical waves. However, such sources are merely mathematical conveniences and have no real physical significance. It is also possible to formulate scalar diffraction theory in a framework that closely resembles the theory of linear, invariant systems. If the complex field distribution of at a center frequency is Fourier-analyzed across any plane, the various spatial Fourier components can be identified as plane waves traveling in different directions away from that plane. The angular spectrum method is such a technique, which involves expanding a complex wave field into a summation of infinite number of plane waves. The field amplitude at any other point (or across any other parallel plane) can be calculated by adding the contributions of these plane waves, taking into account the phase shifts they have undergone during propagation [16].

Electromagnetic fields are described as a superposition of plane waves and evanescent waves which are physically intuitive solutions of Maxwell's equations. The angular spectrum representation is found to be a very powerful method for the description of wave propagation. Analytically, the angular spectrum approach is shown to be equivalent to the Huygens convolution [15]. On the other hand, the angular spectrum picture has the advantage of being more intuitive and free from some of the subtle difficulties of boundary conditions [16]. It also leads to more robust and trouble-free numerical calculations of diffraction. Fig. 1.2 describes the propagation of a plane-wave component in the angular spectrum.

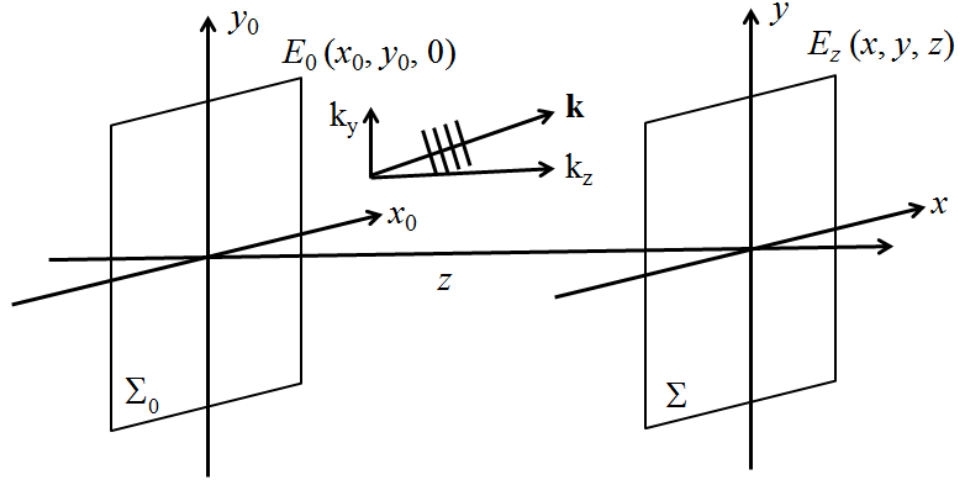


Figure 1.2. Propagation of a plane-wave component in the angular spectrum.

Consider an input field $E_0(x_0, y_0)$, its Fourier transform can be written as

$$A_0(k_x, k_y) = \mathbf{F}\{E_0\} = \frac{1}{2\pi} \iint_{\Sigma_0} dx_0 dy_0 E_0(x_0, y_0) \exp[-i(k_x x_0 + k_y y_0)] \quad (1.6)$$

where k_x, k_y are the x and y components of the propagation vector. According to the basic principle of Fourier transform, A_0 describes the amplitudes of various plane-wave components that comprise the input pattern. The input field $E_0(x_0, y_0)$ is can also be written as the inverse Fourier transform of the angular spectrum:

$$E_0(x_0, y_0) = \mathbf{F}^{-1}\{A_0\} = \frac{1}{2\pi} \iint dk_x dk_y A_0(k_x, k_y) \exp[i(k_x x_0 + k_y y_0)] \quad (1.7)$$

where \mathbf{F}^{-1} is the reverse Fourier transform operator. The complex exponential $\exp[i(k_x x_0 + k_y y_0)]$ is the projection on the (x_0, y_0) plane of a plane wave propagating along the wave vector $\mathbf{k} = (k_x, k_y, k_z)$, where $k_z = \sqrt{k^2 - k_x^2 - k_y^2}$. Thus the input field $E_0(x_0, y_0)$ can be viewed as a projection of many plane-wave components propagating in various directions

$\mathbf{k} = (k_x, k_y, k_z)$, with complex amplitude of each component given by $A_0(k_x, k_y)$. After propagation over a distance z , each plane-wave component acquires a phase factor $\exp(ik_z z)$, so that the output field is given by

$$E(x, y, z) = \frac{1}{2\pi} \iint dk_x dk_y A_0(k_x, k_y) \exp\left[i(k_x x + k_y y + k_z z)\right] \quad (1.8)$$

which is an inverse Fourier transform of $A_0(k_x, k_y) \exp(ik_z z)$, so it can also be written as

$$\begin{aligned} E(x, y, z) &= \mathbf{F}^{-1} \left\{ A_0(k_x, k_y) \exp(ik_z z) \right\} \\ &= \mathbf{F}^{-1} \left\{ A_0(k_x, k_y) \exp\left[i\sqrt{k^2 - k_x^2 - k_y^2} z\right] \right\} \\ &= \mathbf{F}^{-1} \left\{ \mathbf{F} \{ E_0 \} \exp\left[i\sqrt{k^2 - k_x^2 - k_y^2} z\right] \right\} \end{aligned} \quad (1.9)$$

There are several important conditions should be noticed. First, the square root factor in the exponent requires that $k_x^2 + k_y^2 \leq k^2$. That is, the diffraction imposes a low-pass filtering of the input spatial frequencies. When $k_x^2 + k_y^2 \geq k^2$, the square root in Eq. (1.9) is imaginary, these wave components are rapidly attenuated by the propagation phenomenon. Such components are called evanescent waves and are quite analogous to the waves produced in a microwave waveguide driven below its cutoff frequency. Only near field probes can access such evanescent field. Second, note that the description is based only on the fundamental properties of Fourier transform, without having to invoke particular boundary conditions. Third, the physical picture of diffraction is constructed from a set of plane waves, which by definition is well-behaved everywhere in space. On the other hand, the Huygens principle and Rayleigh–Sommerfeld theory are all built up from the behavior of spherical waves of point sources, which inherently involves singularities at the point sources. The angular spectrum result is equivalent to the convolution result and it has been proved in [19].

Equation 1.9 allows back-propagation of the field on one plane to another. If the fields are measured on the plane parallel to the antenna aperture or any other planar source, then the wave can propagate back to the source plane. In reality, the fields are not available in the form of continuous functions, but instead are sampled at discrete locations. In the case of uniform sampling, Equation 1.9 would result in discrete rather than continuous Fourier transforms. Equation 1.9 serves as the basis of the ESM algorithm.

To implement Equation 1.9, the measured field on the scanning plane are converted to spatial spectral domain using a 2D fast Fourier transform and multiplied by the phase term to translate the fields back to the source plane. The non-propagating field component can be suppressed in the spectrum domain. The fields on the source plane can be constructed from the spectrum by using an inverse 2D-FFT. The rectangular scanning plane is divided into a grid of $N \times M$ points. The separation of sampling points on the scanning grid is chosen to be less than $\lambda/2$ in order to satisfy the Nyquist spatial sampling criterion [20].

1.2.3. Resolution of Diffraction-Limited System. The resolution of an optical imaging system – a microscope, telescope, or camera – can be limited by factors such as imperfections in the lenses or misalignment. However, there is a fundamental maximum to the resolution of any optical system which is due to diffraction. An optical system with the ability to produce images with angular resolution as good as the instrument's theoretical limit is said to be diffraction limited [21]. This theory can also be applied on the ESM system. The observation of sub-wavelength structures with microscopes is difficult because of the diffraction limit. Electromagnetic field with wavelength λ ,

traveling in a medium with refractive index n and converging to a spot with angle θ will make a spot with radius

$$R = \frac{\lambda}{2n \sin \theta} \quad (1.10)$$

where $n \sin \theta$ in the denominator is called the numerical aperture (NA), which characterizes the range of angles over which the system can accept electromagnetic field. In the ESM system, the resolution of the scanning, height of the scanning plane, and frequency of operation affects the final resolution of the constructed image. Fig. 1.3 shows aperture angle given by the span of the scan plane.

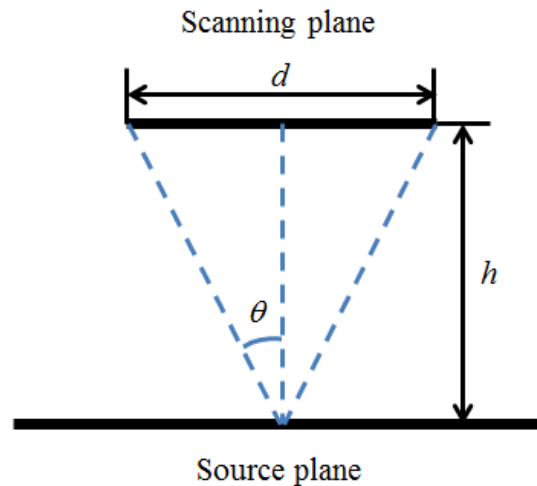


Figure 1.3. Aperture angle of the scanning system.

Here d represents the length of the smallest side, and h is the height of the scanning plane above the DUT.

For an infinitely wide scanning plane, the aperture angle would be 90 degrees, and with air as the medium, the maximum N.A. would be 1. This limits the maximum resolution to $\lambda/2$. This limitation does not allow distinguishing the sources placed closed

as compared to wavelength. For example, with a scanning area of 0.5m x 0.5m, at 1 GHz frequency at a height of 50 cm away from PCB plane, the resolution of the system can be calculated to be 21.2 cm. While with the same scanning system, the resolution of the system for 10 GHz signal can be increased to 2.12 cm. From Equation 1.10, it can be seen that for a given frequency, the resolution of the ESM system can be increased by extending numerical aperture of the scanning system. This can be typically obtained by increasing the scanning area and decrease the height of the scanning plane to the DUT. However, the gain might be very little once the scan plane is much larger than the height. Furthermore, the resolution can be also increased by changing the wave-travelling medium air to high refractive index water.

1.3. CASE 1: SOURCE IDENTIFICATION ON NETWORK SWITCH

Based on the above description of the ESM method, the real hard ware will be used for the EMI source localization. The DUT used for analysis in this section is an off-the-shelf networking device with default software configuration installed.

1.3.1. ESM Measurement Setup. Fig. 1.4 shows the measured total radiated power from the DUT around 10.3125 GHz. This measurement is performed by operating the DUT in a reverberation chamber and measuring the total radiated power using a spectrum analyzer. It can be seen that there are 15 peaks in the spectrum centered around 10.3125 GHz. This section presents a case study on the mitigation of radiation corresponding to only a single frequency i.e. frequency #12 at about 10.312584 GHz. Similarly this analysis can also be extended to other frequency components.

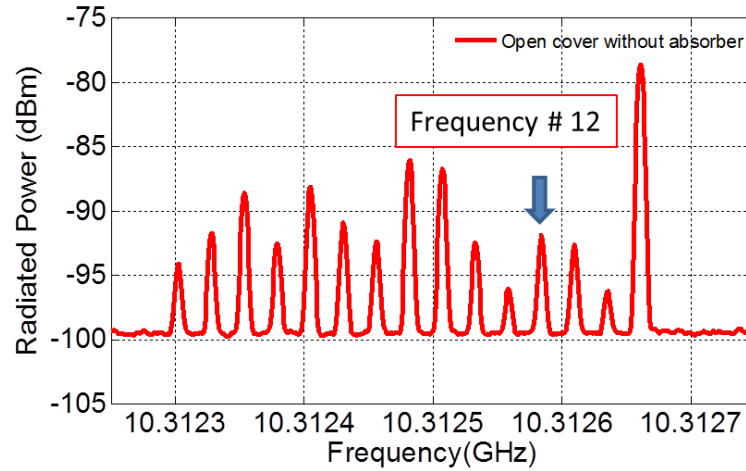


Figure 1.4. Radiation spectrum from the DUT.

The test setup for the hardware measurement using the ESM technique is shown in Fig. 1.5.

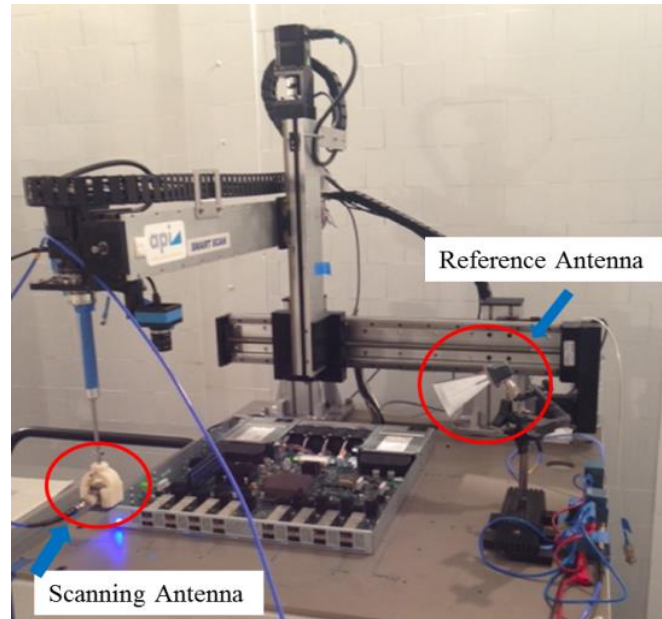


Figure 1.5. ESM test setup for the real hardware measurement.

The DUT with dimensions of $45\text{ cm} \times 40\text{ cm} \times 4\text{ cm}$ is placed at the center of a 3-axis robotic scanning system [22][23]. At this frequency the required maximal spatial scanning step is 1.5 cm. In the actual measurement, a scanning resolution of 7 mm is used. The height of the scanning plane above the PCB is about 8.3 cm, which is between two to three wavelengths at the test frequency.

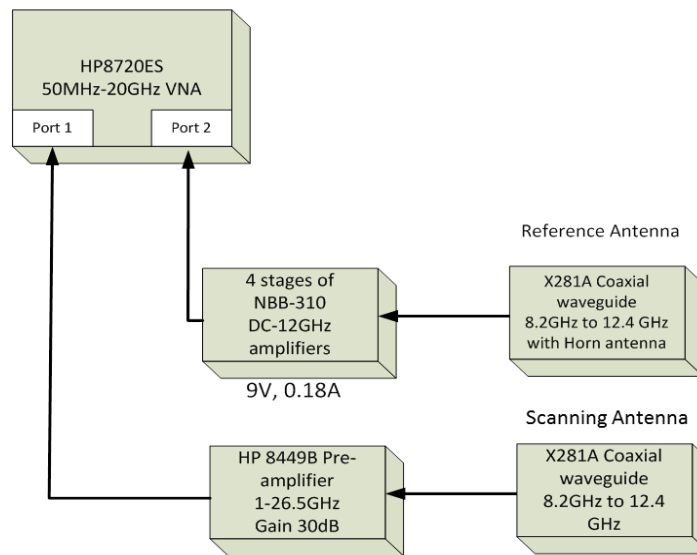


Figure 1.6. The schematic diagram of the ESM measurement setup.

For the ESM method, the tangential E field on the scanning plane is measured with the horn antenna. The measured E field will back propagate to the source plane. A vector network analyzer (VNA) is used in the tuned receiver mode for phase and amplitude measurement. In this mode, one port of the VNA is connected to the reference signal and second port is connected to the signal to be measured. Fig. 1.6 shows the schematic diagram of the ESM measurement setup.

1.3.2. Source Identification with ESM Method. For this measurement, an 8.2-12.4 GHz standard gain horn antenna was used as a reference antenna. This reference

antenna is fixed at a distance away from the DUT in the direction to maximize the output at frequency #12. It is connected to Port 2 of VNA through three cascaded amplifiers each providing 10 dB gain. The scanning antenna is an 8.2-12.4 GHz open-ended waveguide mounted to the arm of the 3-axis robotic scanning system. The output of the waveguide is amplified by a low noise broadband amplifier with a gain of 30 dB before feeding to Port 1 of the VNA. The scanning antenna moves over a scanning plane in a rectangular grid and measures one tangential component of the field in one scan. To measure the orthogonal field component, the antenna is rotated 90 degrees and the scan is repeated.

The image of the DUT is overlapped and aligned with the image of the scanned fields to observe the underlying physical sources of radiation as shown in Fig. 1.7. In this figure, the DUT image has been replaced by the blocks due to proprietary information. Four big black blocks represent the heatsinks in the DUT, 16 smaller blue blocks with the same size represent the physical layer transceiver (PHY), and 8 red rectangular blocks correspond to the optical transceivers on the DUT. As observed, no detailed information about the source of radiation can be obtained from the scanned fields. The quantity plotted is the magnitude and phase of the signal at the VNA Port 1, and the units are dBV and radians respectively.

Also a near-field scanning using a near-field magnetic field probe is performed for frequency #12, as shown in Fig. 1.8. The scanning height is kept as 2 mm above the PCB plane. This would require the probe to retract back and forth while scanning. Here the scanning resolution is kept as 1 mm and only a small area is scanned due to the large time required for scanning. It provides the surface current distribution corresponding to

frequency # 12. Also it contains both the evanescent and propagating wave components. No particularly useful information about the radiating structure can be obtained from the field data. This scan result does not provide enough in sight into the sources of radiation to decide where exactly to place the absorbers to reduce the far-field radiation.

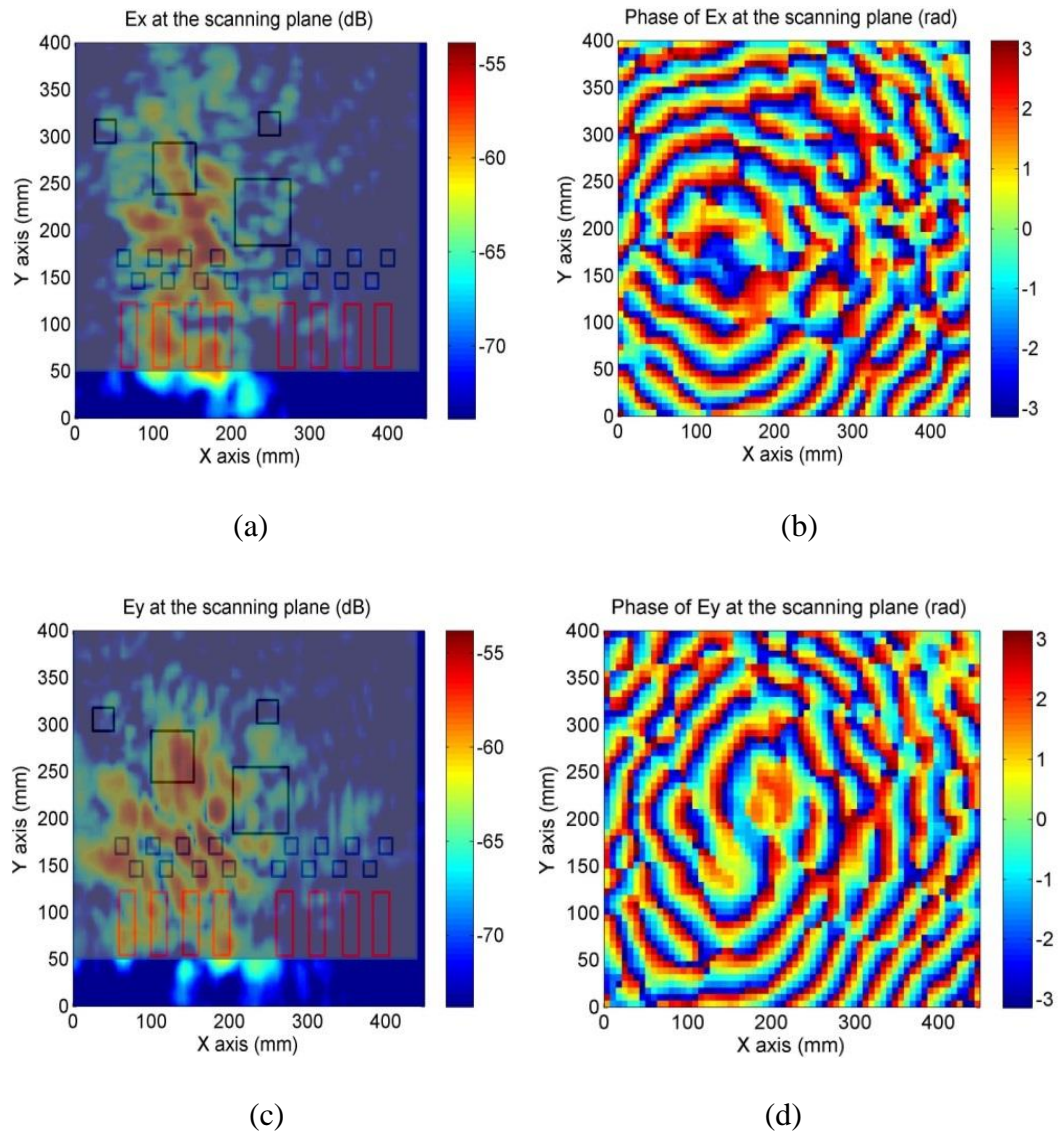


Figure 1.7. Measured E field distribution at the scanning plane. (a) Measured E_x field magnitude in dBV (b) Measured E_x field phase in rad (c) Measured E_y field magnitude in dBV (d) Measured E_y field phase in rad at the scanning plane.

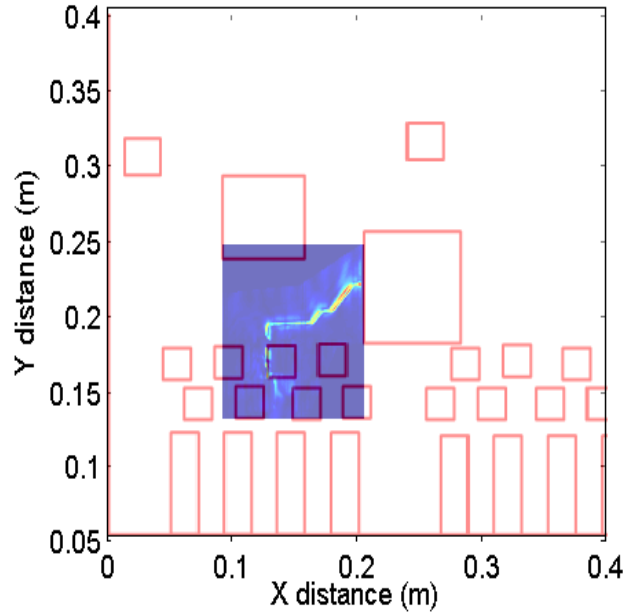


Figure 1.8. Measured total tangential field component with near field scanning.

To identify the source location, ESM algorithm as given by (1) is applied on the scanned fields shown at Fig. 1.7. The reconstructed fields on the source plane for both orientations of the antenna are shown in Fig. 1.9.

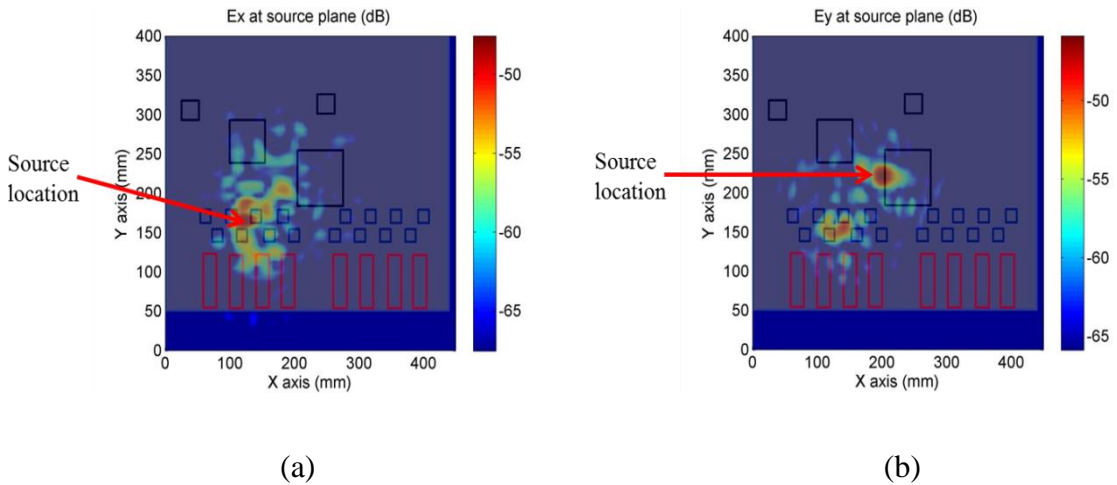


Figure 1.9. Reconstructed E_x (a) and E_y (b) field component magnitude in dBm at the PCB plane.

The resolution of the constructed image can be estimated to be around 1.5 cm according to [24]. Here it can be seen that for the E field in x direction, the source is mainly located near one of the PHYs of the board; and for the E field in y direction, the source is mainly located at the edge of the main heatsink.

1.3.3. EMI Mitigation with Lossy Material. Based on the information obtained from the ESM transformation, suitable position can be identified for placing the absorber material to mitigate the radiation at frequency #12. The properties of the absorber material are defined by the permittivity and permeability of the material and also the size of the material applied. Any use of absorber involves a trade-off between material absorptivity and reflection of the signal [25]. Finding a suitable absorber material for the desired frequency range will improve the effectiveness of the absorber and thus reduce the total volume of the material required. In this work, for frequencies at 10 GHz, a non-conductive, magnetically lossy material (BSR-2) [26] was used for EMI mitigation.

Four pieces of absorber material are placed on the edge of the main heatsink where the hot spot corresponding to the source of radiation can be observed as marked in Fig. 1.9(b). Each piece of absorber material size is 2 cm by 2.8 cm, with the thickness 1 mm. The placement of the absorber material is as shown in Fig. 1.10.

Fig. 1.11 shows the reconstructed image from the source plane, after the absorber materials are added at the source location. The color scale corresponding to the field strength in Fig. 8 is set to be the same as Fig. 6 to facilitate comparison. It can be clearly observed that the field strength at the source location has been greatly reduced due to the effect of the absorber material. This validates the location of the source identified by the ESM algorithm to be accurate.

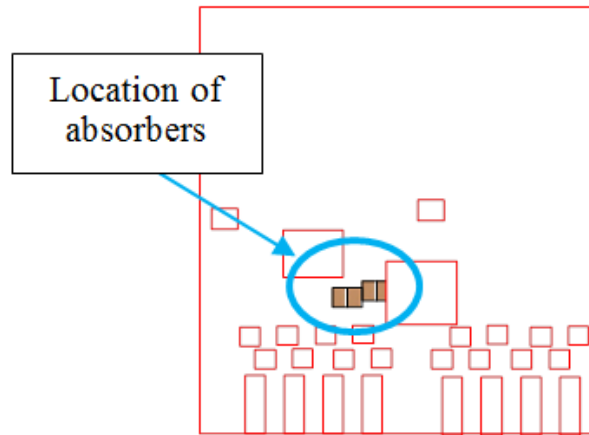


Figure 1.10. 4 pieces of absorbers with the size $2 \times 2.8 \text{ cm}^2$ applied on the source location.

By comparing the reconstructed field strengths in the source plane with and without the absorber material, the maximum value of the source in the x orientation is reduced from -47.6 dB to -53.9 dB , when the absorber material is added; for the y orientation, the maximum value of the source is also reduced from -45.9 dB to -49.9 dB .

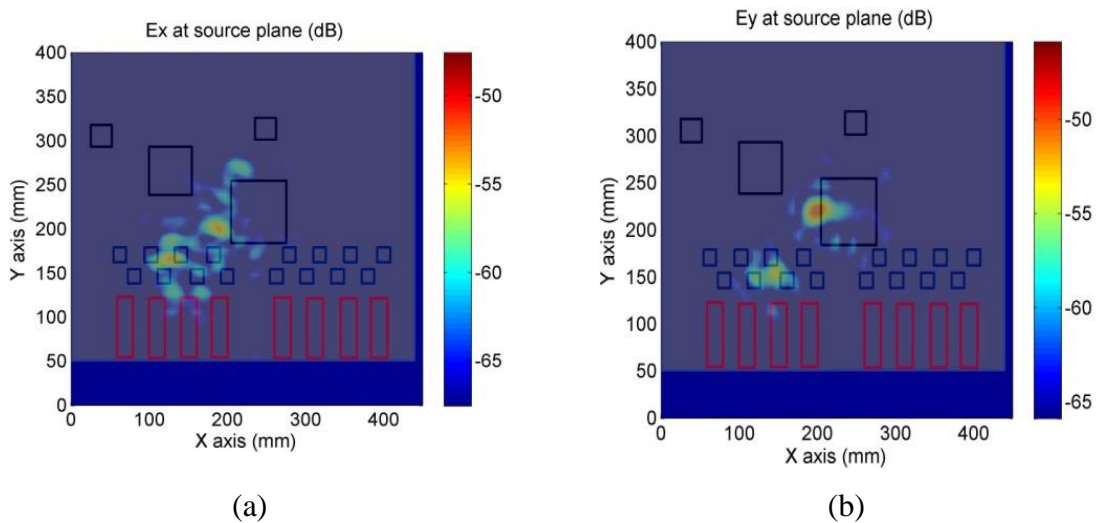


Figure 1.11. Reconstructed E_x (a) and E_y (b) fields at the PCB plane (with absorber).

1.3.4. Total Radiated Power Comparison. As seen from the previous results, it can be observed that the source radiation is reduced by approximately 4 dB when the absorber material is placed at the location identified by the ESM algorithm. To validate these results in the far-field, a total radiated power measurement (TRP) is performed on the DUT using a reverberation chamber. The reverberation chamber measurement is widely used for EMI testing and particularly effective in quantifying the total radiated power of the DUT [27]. Fig. 1.12 shows the setup for the TRP measurement of the DUT. A spectrum analyzer is used with center frequency at 10.3125 GHz and the span as 500 kHz. A low noise 30 dB broadband amplifier is used to increase the received signal strength. Fig. 1.13 shows the averaged total radiated power spectrum comparison with and without absorber material.

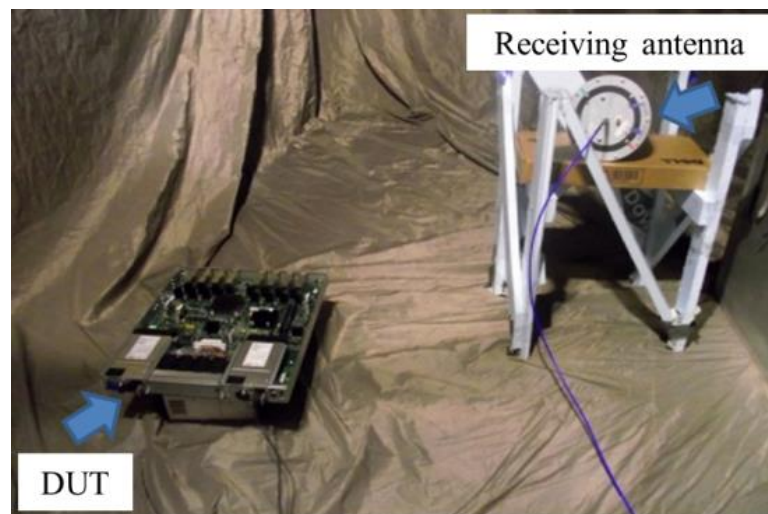


Figure 1.12. Setup for the TRP measurement in a reverberation chamber.

From the Fig. 1.13, it can be seen that the peak value corresponding to frequency #12 has reduced about 4 dB, due to the absorber material, which validates the previous

measurement using the ESM method. But as observed, most of the other frequencies are not affected by the placement of the absorber material. This reconfirms that the location of absorber material determined by the ESM algorithm mainly corresponds to the source of frequency # 12.

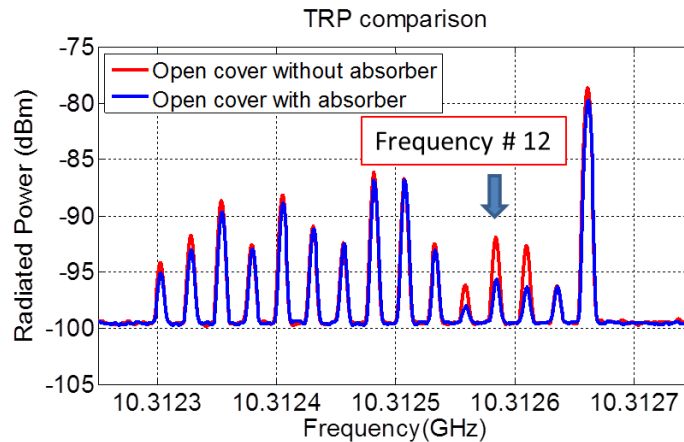


Figure 1.13. TRP spectrums comparison with and without the absorber material.

1.3.5. Conclusion. Using emission source microscopy technique, sources of EMI radiation can be approximately localized on a complex and large system. By placing a suitable volume absorber material on the identified source location, the EMI radiation at 10 GHz from a particular source can be reduced. A TRP measurement using the reverberation chamber validates the reduction of radiation from the identified source. This method can be applied to identify the source of other frequency components as well.

1.4. CASE 2: SOURCE IDENTIFICATION ON COMPUTER SCREEN

Flex printed circuits (FPC) is a technology for assembling electronic circuits by mounting electronic devices on flexible plastic substrates, such as polyimide, PEEK or

transparent conductive polyester film. The flex circuits have lots of advantages, such as: ease for manufacturing or assembly, single-sided circuits are ideal for dynamic or high-flex applications and stacked FPCs in various configurations. However, if the flex printed circuits are bend too much, it will stretches the outside layers of the bend and compresses the inside layers. Compression can cause wrinkles in the cover coat on the inside of the bend. It can also ripple conductors. Cover wrinkles often result in delamination, and rippled conductors can lead to cracks. This will cause the EMI problems in the real production.

1.4.1. Introduction of the Flex Printed Circuit on Computer Screen. Fig. 1.14 shows the back side of a computer screen. The data flex cable connects the main board to another PCB on the screen. For the data flex cable, it has been covered with the conductive tape. It can be seen from the picture that the flex printed circuit has been bend to connect the two PCB together. The ESM methodology will be used to investigate the radiation of the flex cable.

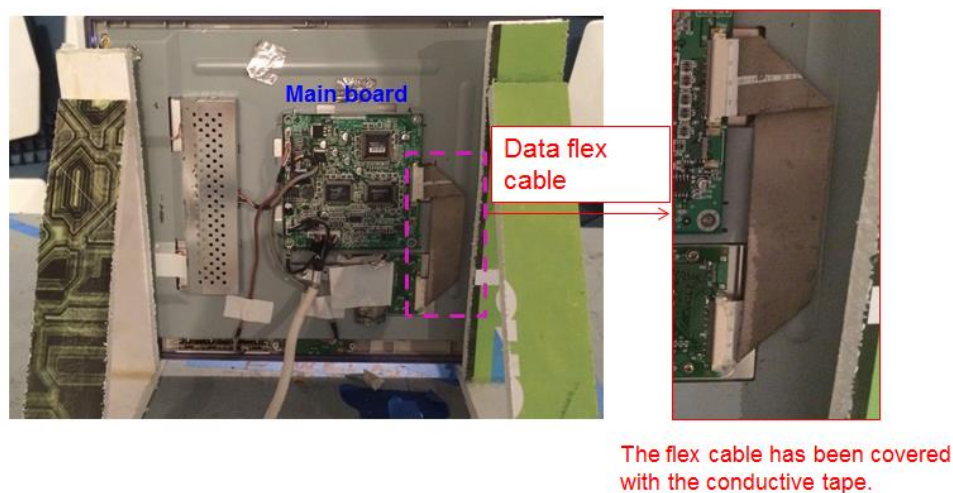


Figure 1.14. Back side of the computer screen.

1.4.2. ESM Measurement Setup with Manually Scanning System. Fig. 1.15 shows the sketch diagram of the Emission Source Microscopy Technology. The distance of antenna 1 to the DUT flex cable is about 43 cm. The antenna 2 is placed close to the flex cable as reference. At first, A/B value (as captured by the VNA) is measured and stored by Matlab code. Next the B value is measured to calculate the magnitude value on the scanning plan. In this measurement, only 1 direction is scanned (Ex) which is enough for the source identification. Fig. 1.16 shows the manually scanning setup above the computer screen. The scanning hardware is used to move the antenna on the scanning plane and it collects fields over a synthetic aperture. Both of the amplitude and phase information of the field in the scanning place can be collected. The fields can be translated by transforming the fields from spatial to spatial frequency domain and then propagate them back to the source plane. On the source plane, they are back converted to the spatial domain to retrieve the focused image. The focused image on the source plane provides the information about the sources of radiation.

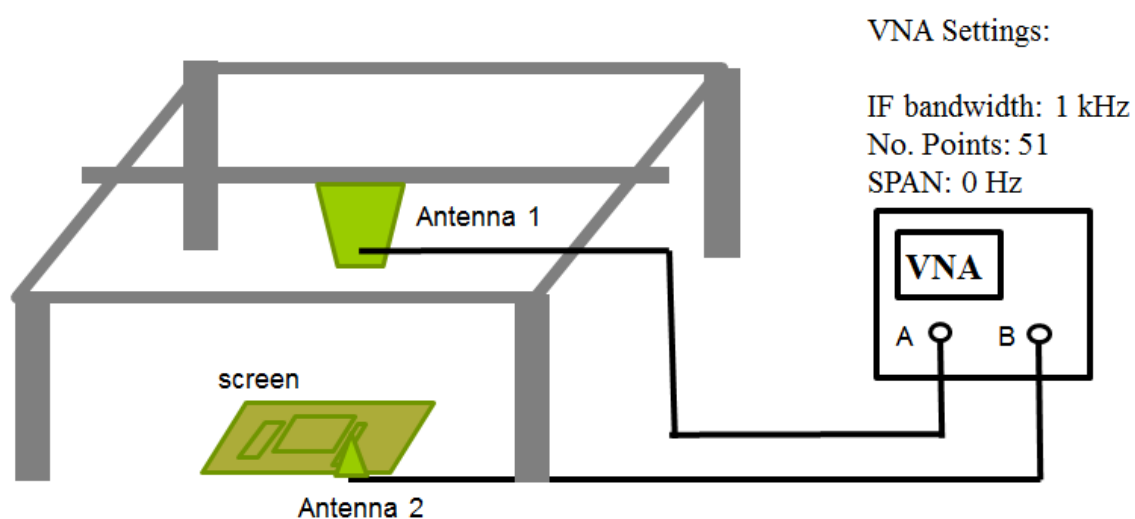


Figure 1.15. Sketch diagram of the Emission Source Microscopy technology.

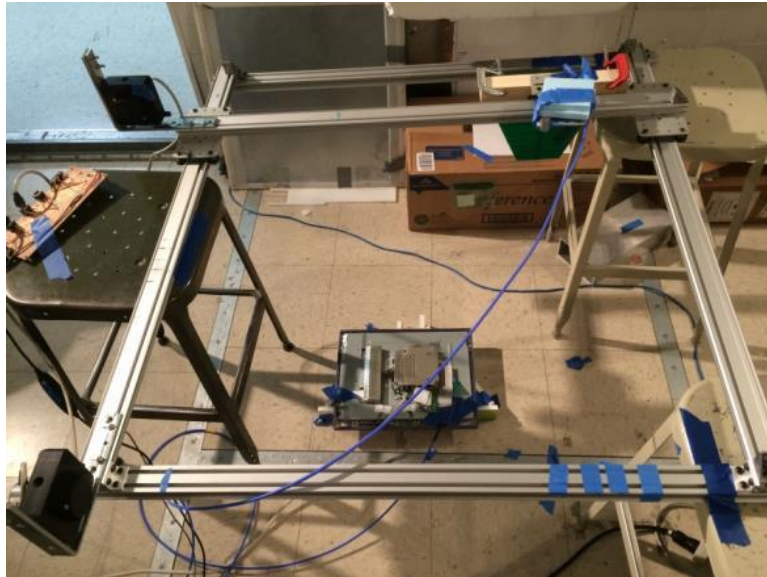


Figure 1.16. ESM setup on the computer screen.

1.4.3. ESM for the Source Identification. Using the method described above the computer screen has been measured for the source identification. Fig. 1.17 shows the back side of the computer screen. The Antenna 2 is fixed on the flex cable as the reference for the phase measurement.

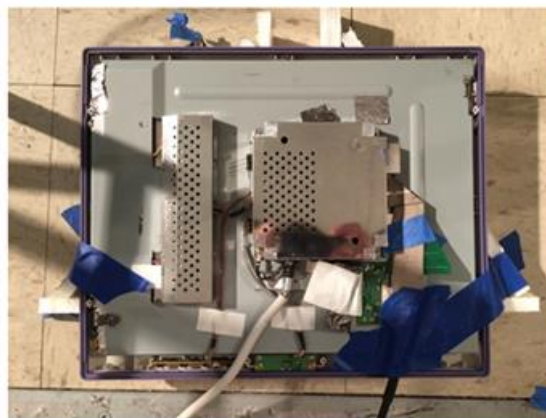


Figure 1.17. Back side of the computer screen.

Fig. 1.18 shows the magnitude and phase information on the scanning plane at 1514 MHz. The distance from the antenna to the DUT is 43 cm. Using the ESM method, the focusing plane (DUT plane) field can be back propagated from the measured plane, which is shown in Fig. 1.19. In the focusing plane field, it can be seen that the hot point is located at the flex cable of the computer screen. However, since the frequency is around 1.5 GHz, the hot point size is about 20 cm by 20 cm.

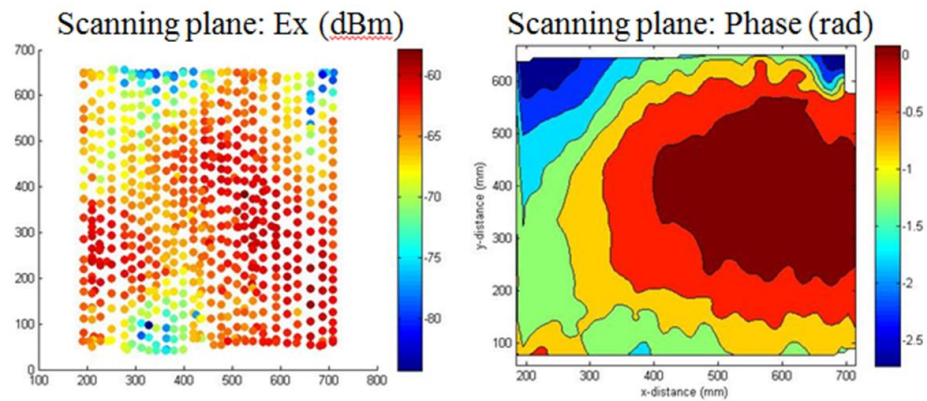


Figure 1.18. Scanning plane magnitude and the phase distribution (at 1514 MHz).

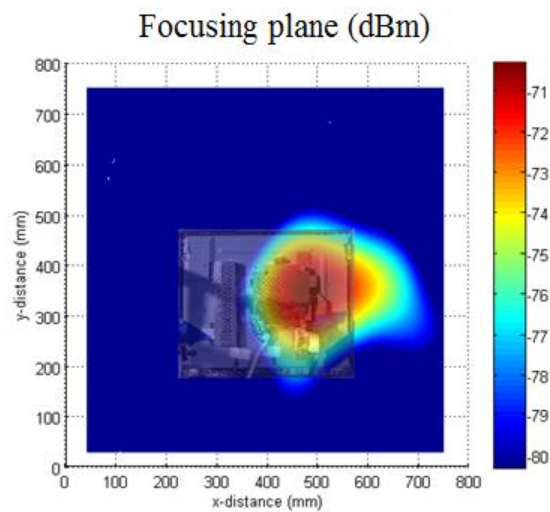


Figure 1.19. Focusing plane field distribution (at 1514 MHz).

From the discussion in Section 1.2.3, it can be seen that, to increase the resolution of the focusing plane, the distance between the scanning plane and the source plane can be decreased. Fig. 1.20 shows that the scanning distance has been reduced from the 43 cm to 25 cm by adding the foam underneath of the computer screen. The scanning area is about 50 cm by 50 cm. From equation 1.10, it can be calculated that the resolution will be increased from 19.7 cm to 14.0 cm after changing the distance from the 43 cm to 25 cm.

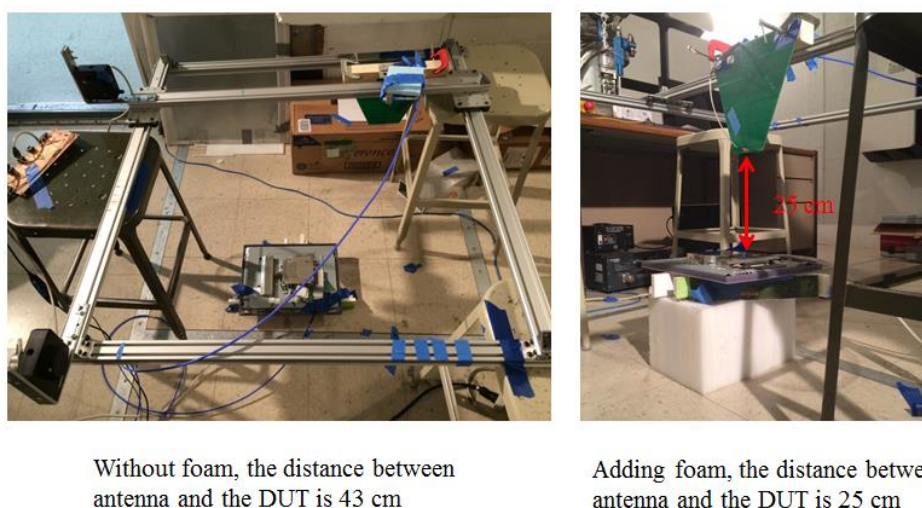


Figure 1.20. Reduce the distance between the antenna and the DUT to 25 cm.

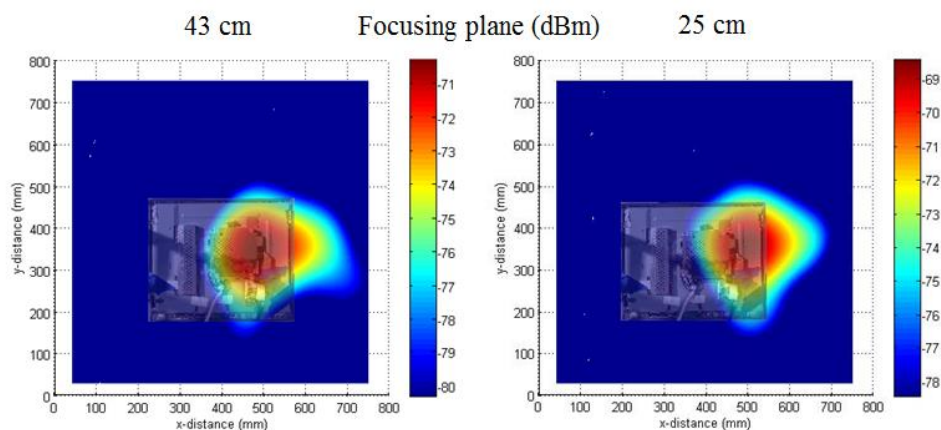
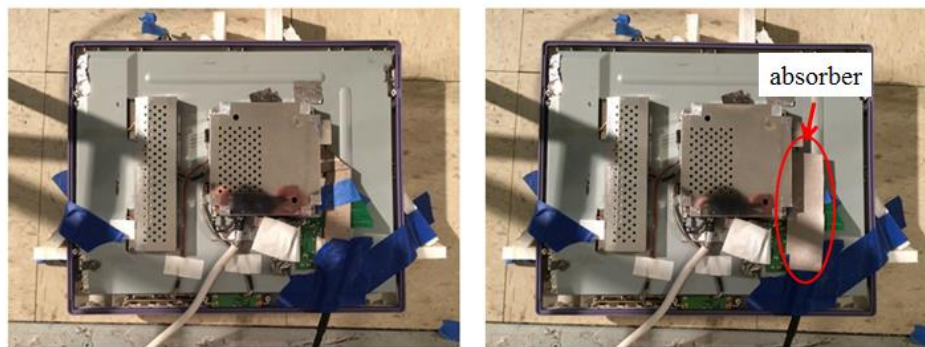


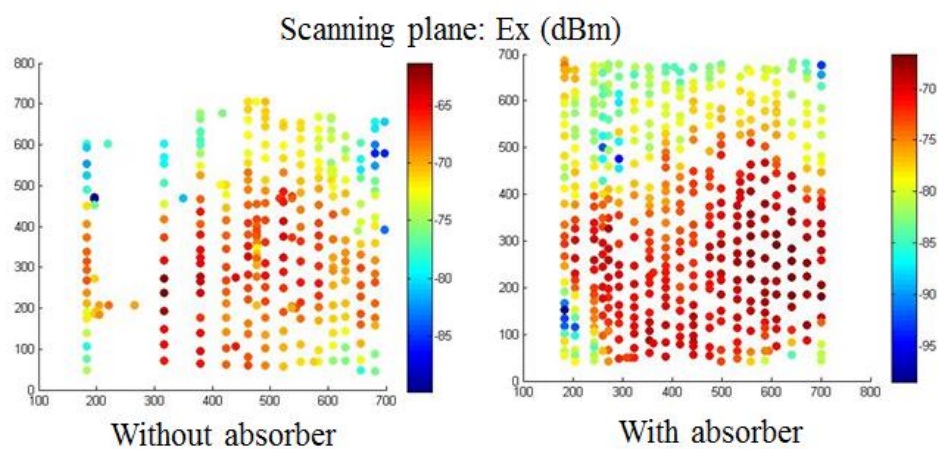
Figure 1.21. Focusing plane field distribution with different scanning heights.



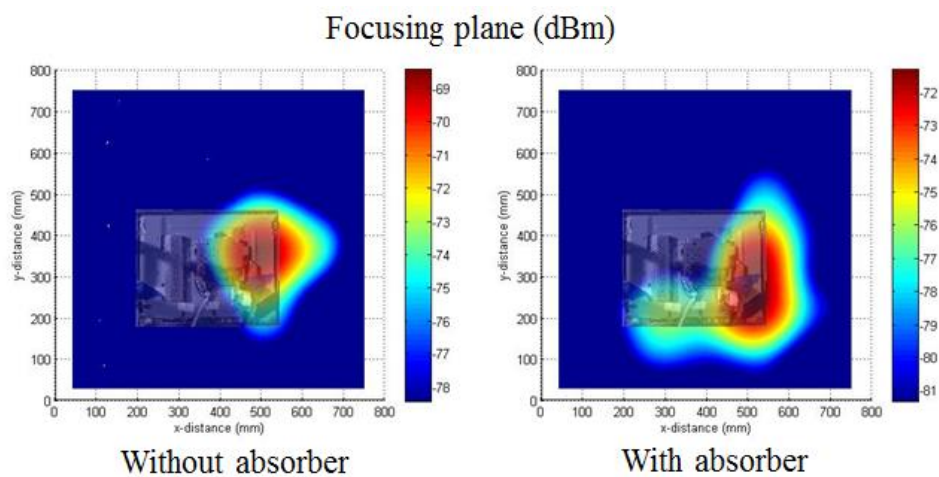
Without absorber

With absorber cover the flex cable

(a)



(b)



(c)

Figure 1.22. Field comparison with and without absorber applied.

Fig. 1.21 shows that, after changing the scanning distance from the 43 cm to 25 cm, the hot point in the focusing plane has been reduced in size (Even the reduction is not too much). It can still see that the source is very close to the flex cable.

After identifying the source location, the lossy material is applied on the flex cable of the computer screen to reduce the EMI radiation. Fig. 1.22 compares the magnitude distribution with and without absorber on the scanning and focusing plane at 1514 MHz. The distance between scanning plane to the DUT is 25 cm. After adding the lossy material on the flex cable, the maximal value on the scanning plane has reduced about 6 dB. On the focusing plane, the maximal value has reduced about 3 dB. This difference might be due to the measurement error in the system.

1.4.4. Far Field Measurement of the Computer Screen in the 3 m Chamber.

To confirm the conclusion in the ESM method, a far field measurement has been performed in the 3 m chamber. Fig. 1.23 shows the far field measurement of the computer screen in the 3m chamber. The log periodic antenna is used in this measurement. The distance from the antenna to the DUT is 0.85 m. The antenna height to the ground is 1 m and it is vertical polarized during the measurement. The DUT is placed in a turntable table. Outside of the chamber, the spectrum analyzer is connected to the log periodic antenna through an amplifier. This measurement is used to confirm the lossy material performance in the far field measurement and also can be used to verify the ESM method for the source identification. This is the reason that only one direction was measured in the chamber.

Fig. 1.24 shows the far field comparison of the screen with and with absorber. The yellow curve is the radiation without absorber and the blue curve is the case with

absorber. It can be seen that radiation at 1514 MHz drops about 4.1 dB after adding the absorber. This result confirms that the ESM method find the right source location on the computer screen, and the lossy material applied on the flex cable can reduce the EMI radiation at this frequency.

SA Settings:

CF: 1.5143 GHz
RBW: 10 Hz
SW Points: 5001
Attenuation: 0 dB
SPAN: 2 kHz



Figure 1.23. Far Field measurement of the computer screen in the 3 m chamber.

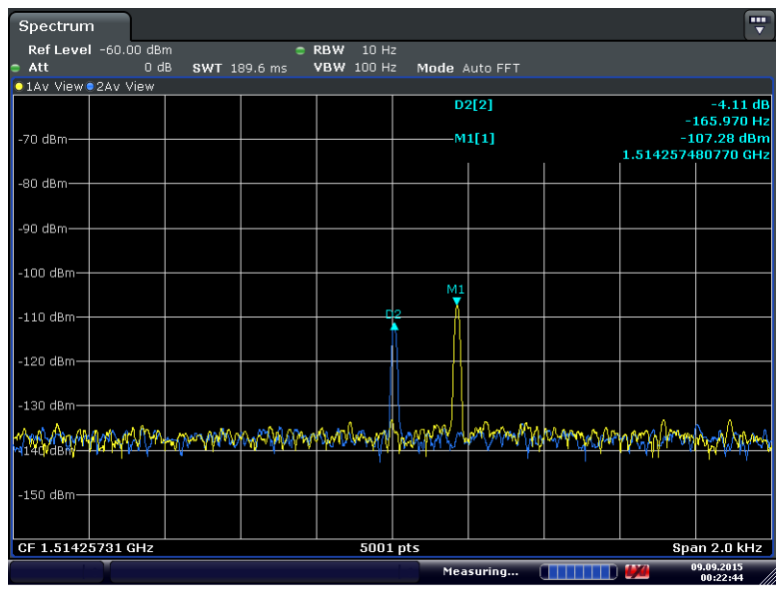


Figure 1.24. Far Field comparison with and without absorber.

From the figure 1.24, it can be seen that the radiation peak at 1514 MHz has about 200 Hz shift. This is because after adding the lossy material on the flex cable, the temperature on the flex cable will change and it will cause the radiation peak shift.

1.4.5. Conclusion. The ESM methodology has been performed on a computer screen. From the back propagated field on the source plane, it can be determined that the main radiation source is coming from the flex cable of the computer screen. From the ESM results, it can be seen that the maximal value of the E_x field on the focusing plane can reduced about 3 dB at 1514 MHz. To verify the ESM method for the source identification, the 3 m chamber measurement has been performed. It can be seen that maximal value of the far field in the vertical polarization at 1514 MHz drops about 4.1 dB after adding the absorber on the flex cable.

1.5. CASE 3: RADIATION FROM HEATSINKS AND MITIGATION USING ABSORBING MATERIALS

heatsink is a passive heat exchanger that transfers the heat generated by an electronic or a mechanical device into a coolant fluid in motion. It has been commonly used in the complicated system to reduce the thermal effect. At current operating frequencies of electronic integrated circuits in tens of GHz heatsinks become effective antennas and can contribute to EMI problems.

1.5.1. Introduction of the Heatsink Radiation. There are many works on heatsink radiation mitigation, such as designing the heatsink structure [29] and grounding the heatsink [30], but it is still very difficult to effectively reduce the radiation of heatsink over a broadband frequency range. Absorbing materials added on the heatsink system can help to reduce the radiation over a broadband frequency range. Specially designed lossy

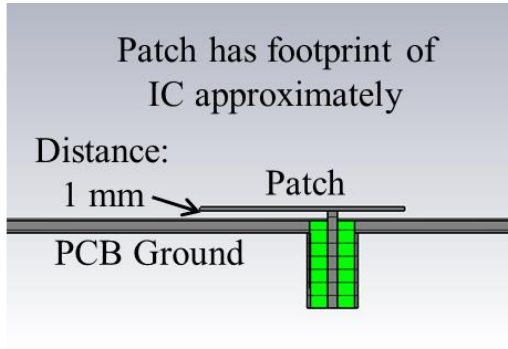
materials with good heat transfer characteristics can be applied between an IC and a heatsink, in such case absorbing material is placed closest possible to the interference source.

1.5.2. Heatsink Modeling and the S-parameters Comparison. The CST simulation model and the experimental test setup of the heatsink system are shown in Fig. 1.25. A metal patch with the common size of an IC chip is used to emulate an IC radiation, as show in Fig. 1.25 (a)-(b). The distance from the patch to PCB ground is 1 mm. In Fig. 1.25 (c)-(d), the heatsink is installed over the surface of the metal patch, and the air gap from the heatsink to the PCB ground is 3 mm. To evaluate the heatsink radiation and lossy material application effectiveness, a short monopole probe is placed in 5 cm from the heatsink. To mitigate the heatsink radiation, the picture frame shape absorbing material is added on the bottom of the heatsink, as shown in Fig. 1.25 (e)-(f). The wall thickness of the lossy materials is 4.7 mm and height is 3 mm.

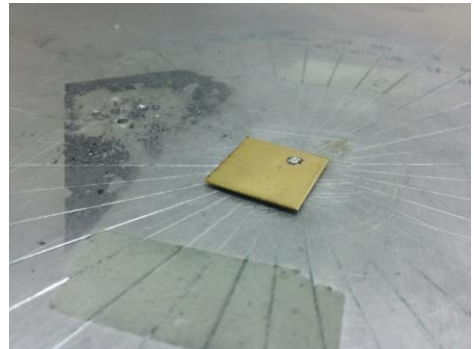
The simulated and measured S_{11} and S_{21} parameters in frequencies range from 100 MHz to 20 GHz with and without the absorbing materials are presented in Fig. 1.26 and Fig. 1.27.

The S_{21} transmission parameter depicts the radiation behavior of the heatsink system. As shown in Fig. 1.27, the S_{21} parameter drops almost 20 dB over the frequency range from 10 GHz to 20 GHz by adding the lossy material on the bottom of the heatsink. The data shown in Fig. 1.26 and Fig. 1.27 consists of 4 datasets – simulation and measurement results for S_{11} and S_{21} demonstrating absorbing material effect on reflection and transmission coefficients respectively. While the results strongly indicate trends of

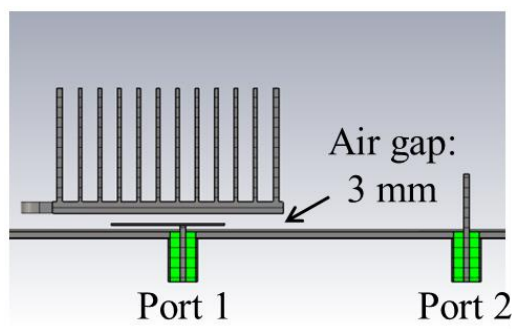
heatsink radiation suppression FSV validation of the data is used to estimate model accuracy.



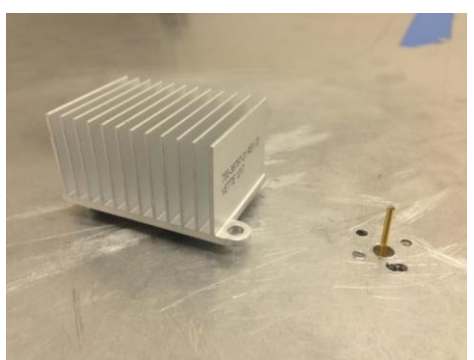
(a)



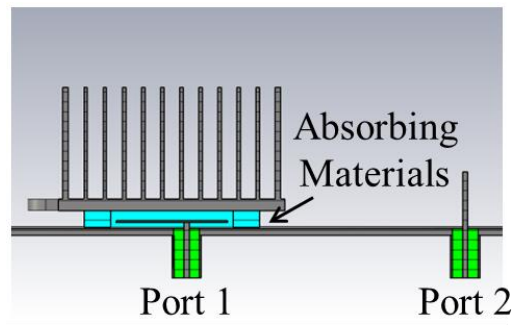
(b)



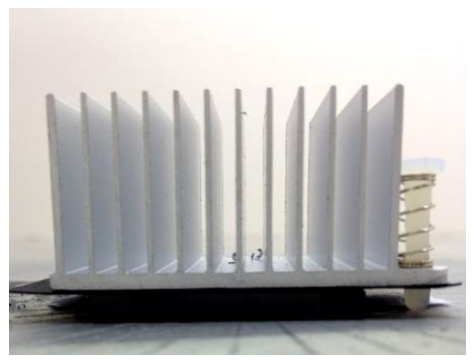
(c)



(d)



(e)



(f)

Figure 1.25. The simulation model and the experiment measurement setup of the heatsink system.

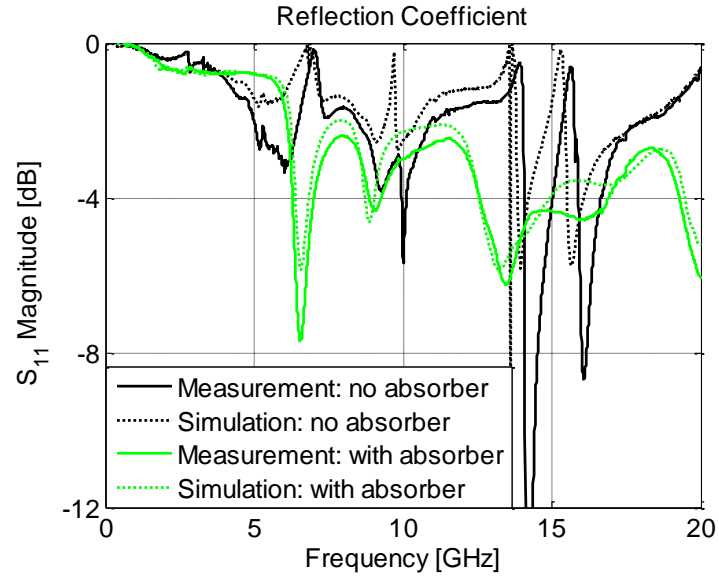


Figure 1.26. The simulated and measured S_{11} parameter of the heatsink with and without the absorbing materials.

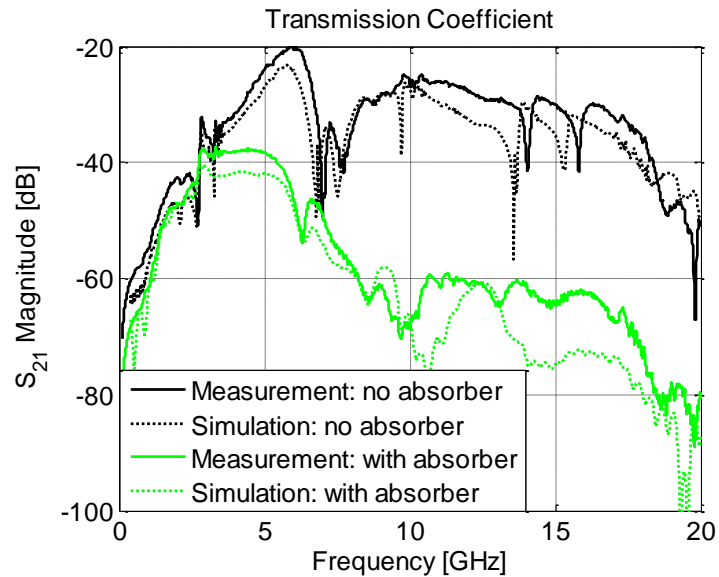


Figure 1.27. The simulated and measured S_{21} parameter of the heatsink with and without the absorbing materials.

Fig. 1.28 shows GDMc histograms for the considered data sets. Major part of the histogram content is in Good-Very Good region. The Grade-Spread data for GDM of all the cases is shown in the Table 1.1.

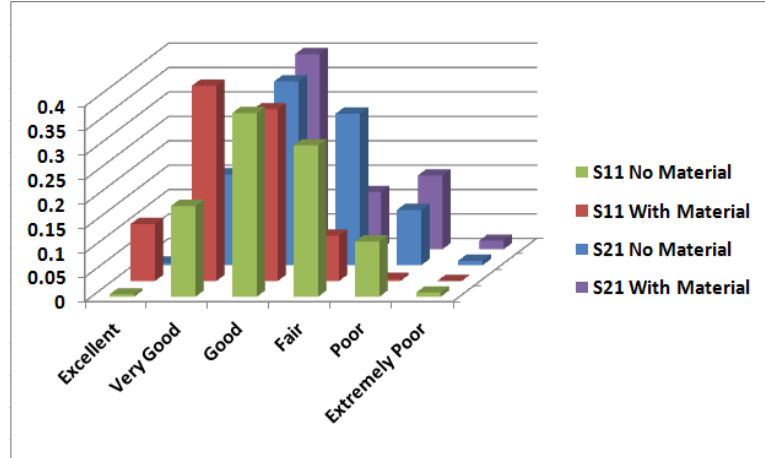


Figure 1.28. Feature selection validation results with global difference measure confidence histograms for heatsink application.

Table 1.1. Spread – Grade data for the heatsink application example for Global Difference Measure.

Data set	Grade	Spread
S ₁₁ No Material	5 (Poor)	5 (Poor)
S ₁₁ With Material	3 (Good)	3 (Good)
S ₂₁ No Material	3 (Good)	4 (Fair)
S ₂₁ With Material	5 (Poor)	4 (Fair)

1.5.3. Heatsink Total Radiation Measurement. The effectiveness of the absorber can be intuitively validated by near-fields scanning around hot spots [31]-[32]; however, the suppression of radiation can also be more efficiently assessed in terms of the total radiated power, which is measured in the reverberation chamber. According to [33], the total transmitted radiated power of the heatsink P_T^H can be found as:

$$\langle P_T^H \rangle = \frac{\langle P_T^A \rangle}{\langle P_R^A \rangle} \langle P_R^H \rangle \quad (1.11)$$

The measurement is done in two stages. During the first stage (calibration) the power P_T^A is applied to one of the calibration antennas and the power P_R^A is received by

another antenna. During the measurement, the power emitted by the heat sink (P_{R^H}) is measured by one of the antennas used in the calibration. In formula (2), the symbol $\langle \rangle$ denotes averaging over the range of steerer positions. If the measurements are performed with VNA excitation, and well-matched antennas are used, equation (2) can be changed to [34]:

$$\langle P_T^H \rangle \approx \frac{\langle |S_{21}^H|^2 \rangle}{\langle |S_{21}^A|^2 \rangle} \langle P_{in}^H \rangle \quad (1.12)$$

where S_{21}^A is the transmission coefficient between two calibration antennas (shown in Fig. 10) and S_{21}^H is the transmission coefficient between the heat sink and one of the antennas (shown in Fig. 11), and P_{in}^H is the assumed power applied to the heatsink.

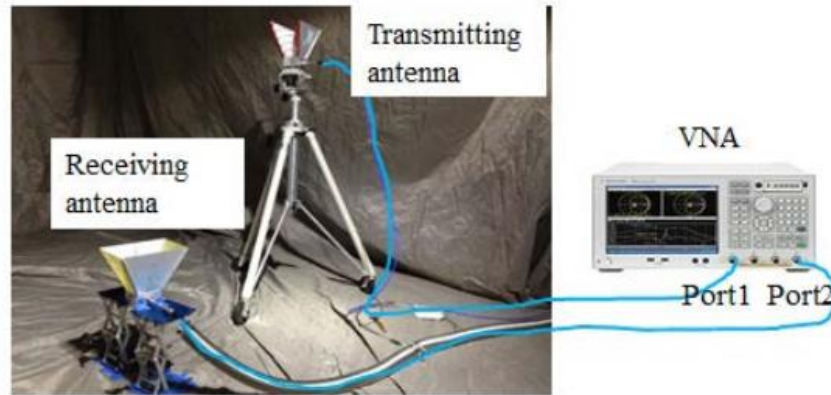


Figure 1.29. Setup for the chamber calibration.

The simulated and measured values of the TRP (total radiation power) are shown in Fig. 1.31. The measured TRP was renormalized to 1 Watt excitation for the comparison purposes. The curves of EMI reduction due to the added lossy material obtained in measurement and simulation are shown in Fig. 1.32. The difference between

the measured and simulated TRP reduction figures does not exceed 6.5 dB, and is 2.3 dB on average. At the same time, it should be noted that the measured and calculated TRP reduction curves are specific to the particular excitation type, such as a patch antenna, and might be different for different excitation mechanisms (e.g., a magnetic loop or a monopole).

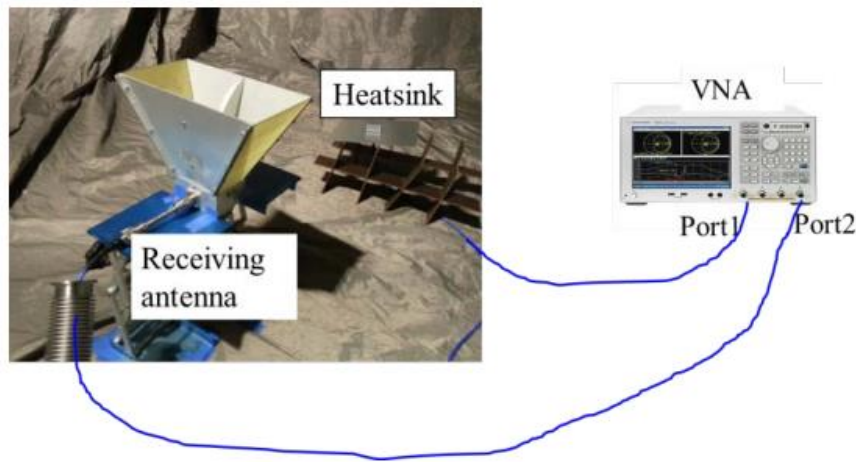


Figure 1.30. Setup for the total radiated power measurement of the heatsink.

The simulated and measured values of the TRP (total radiation power) are shown in Fig. 1.31. The measured TRP was renormalized to 1 Watt excitation for the comparison purposes. The curves of EMI reduction due to the added lossy material obtained in measurement and simulation are shown in Fig. 1.32. The difference between the measured and simulated TRP reduction figures does not exceed 6.5 dB, and is 2.3 dB on average. At the same time, it should be noted that the measured and calculated TRP reduction curves are specific to the particular excitation type, such as a patch antenna, and might be different for different excitation mechanisms (e.g., a magnetic loop or a monopole).

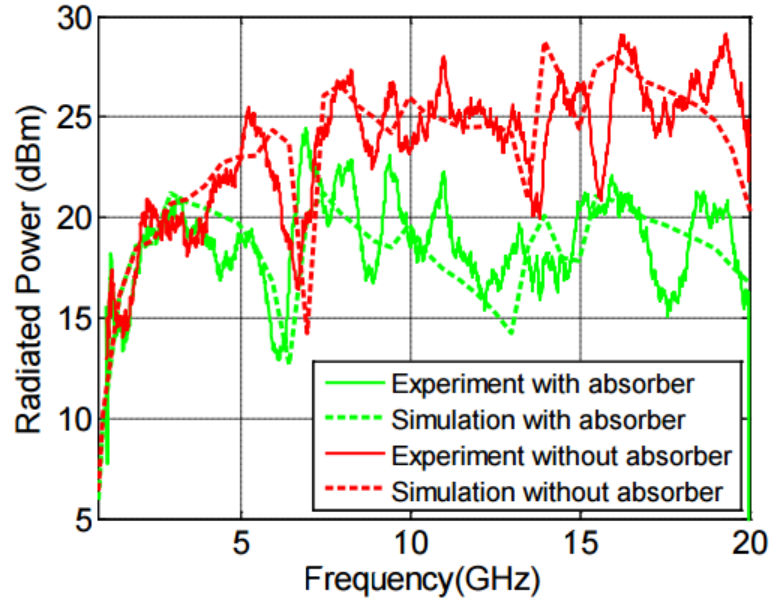


Figure 1.31. Comparison of simulated and measured results of radiation power.

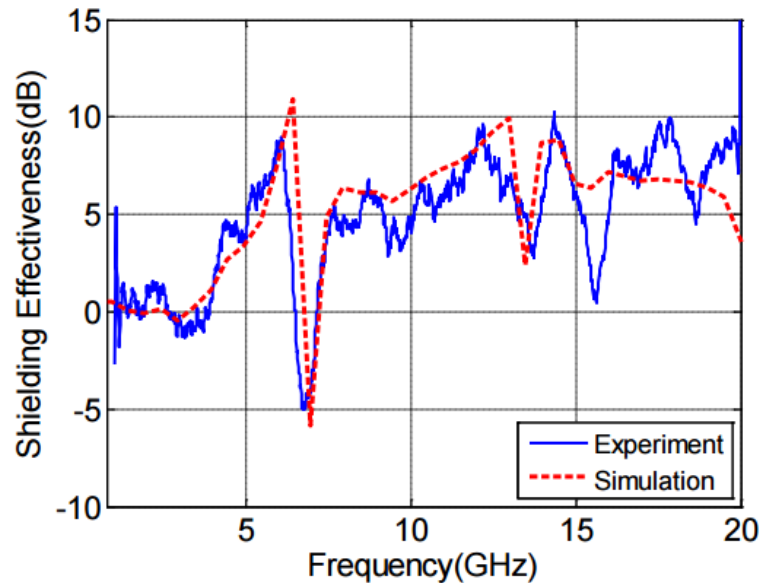


Figure 1.32. Comparison of simulated and measured results of total radiation reduction.

1.5.4. Near Field to Far Field Transformation. Near field (NF) to far field (FF) transformation techniques are widely used for antenna radiation problems. In principle, the transformation can be performed if all sources are confined in the scanned area using

Huygens' Principle, which requires knowledge of the phase and magnitude data of measured fields [32].

Usually, NF to FF transformation technique relies on comprehensive NF-distribution information, which includes both amplitude and phase data. Some of the techniques can overcome difficulties associated with the phase measurement by using NF-scan magnitude-only data recorded on two separate planes, and then retrieve relative information from the mathematical processing of the field distribution difference over the considered planes [35].

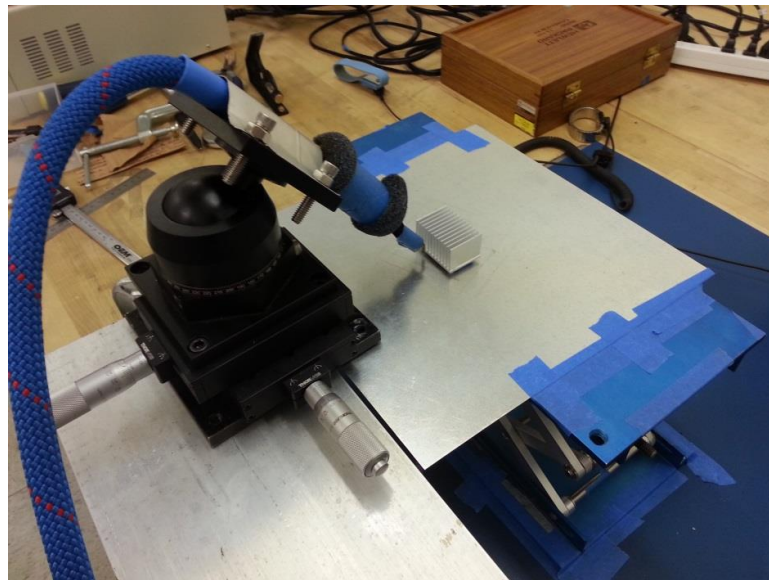


Figure 1.33. Near field scanning setup for the heatsink radiation.

Experimental validation of NF to FF transformation using a limited set of data was performed using the heatsink fixture shown in Fig. 1.33. The equivalent field source can be determined by using the near field scanning methodology, then the field transformation procedure for the IC/Heatsink structure can be used to obtain the total radiation power of the heatsink. Figure 1.34 shows the self-made coaxial probe, which

can be used to capture the E_z components of the near field of the heatsink. The probe is moved along the sides of the heatsink to scan the E-field. The distance of the Probe to the heatsink keeps 1 mm.

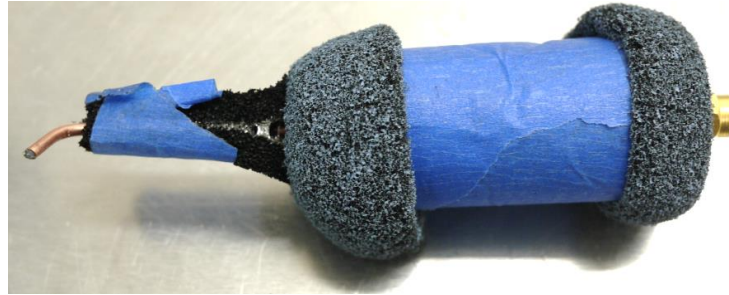


Figure 1.34. E field probe used for the near field scanning setup.

Figure 1.34 shows the self-made coaxial probe, which can be used to get the E_z components of the near field of the heatsink. The probe is moved along the sides of the heatsink to scan the E-field. The distance of the Probe to the heatsink keeps 1 mm.

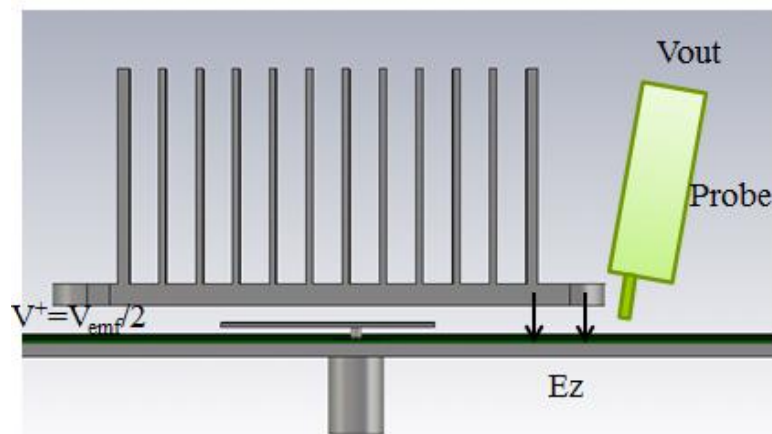


Figure 1.35. The CST model of the heatsink.

Figure 1.35 shows the CST model of the heatsink. The output voltage of the probe is proportional to the vertical component of the E-field

$$V_{out} = A \cdot E_z^c \quad (1.13)$$

On the other hand, the transmission from the heatsink port to the probe output is

$$S_{21}^c = \frac{V_{out}}{V_{emf} / 2} \quad (1.14)$$

Therefore the probe factor is calculated as

$$A = \frac{S_{21}^c V_{emf}}{2E_z^c} \quad (1.15)$$

In the CST, 1 W incident power corresponds the 14.1 V voltage in V_{emf} .

Figure 1.36 shows the measured prober factor over the frequency range from 10 MHz to 20 GHz at different positions around heatsink. The red curve shows the mean value calculated from all of the measurement at different points.

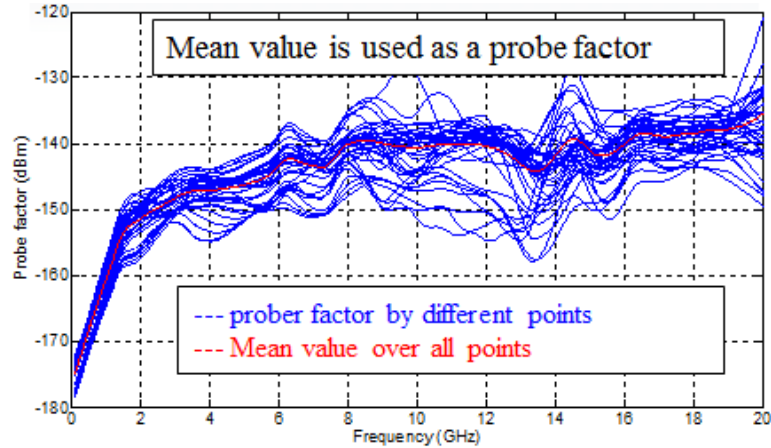


Figure 1.36. E field probe used for the near field scanning setup.

After getting the prober factor, the E_z component around the heatsink can be calculated based on the S_{21} parameters at each point. Then the E_z field can be imported into the CST model as the source of the excitation. The PEC block is added in the bottom

of the heatsink, which is needed to restore (obtain the missing) the H field of the source. Based on this model the total radiated power of the heatsink can be calculated.

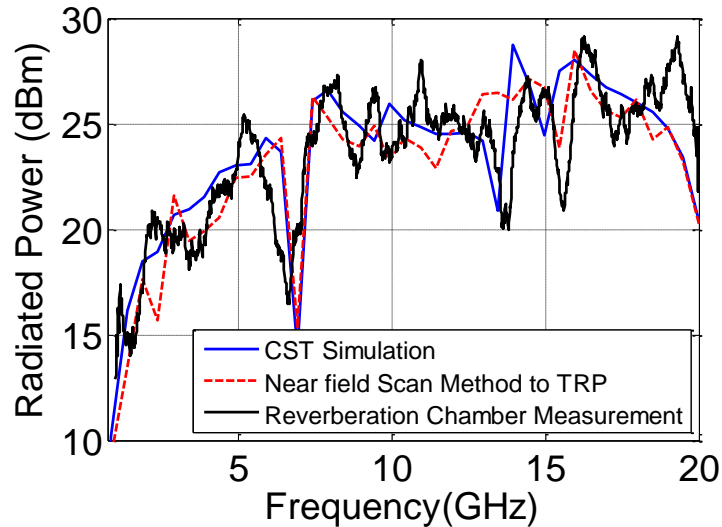


Figure 1.37. Comparison of the total radiated power results with different methodologies.

Figure 1.37 compares the comparison of the total radiated power (TRP) with different methodologies. The blue curve shows the TRP results with full wave simulation, the red dash curve shows the NF to FF calculation results, and the black curve shows the TRP measurement results from the reverberation chamber. From the comparison, it can be seen that both full-wave simulation and NF to FF method calculation results agree well with the reverberation chamber measurement results up to 20 GHz.

1.5.5. Conclusion. In this section, absorber material is applied on the heatsink bottom to reduce the radiation of the heatsink structure. The EMI performance of the absorber material has been predicted by the CST simulation. It has been also validated by the total radiated power measurement in the reverberation chamber. Furthermore, the NF to FF transformation techniques has also been performed on the heatsink radiation

problem. The measured NF data has been imported into CST as the source to calculate the total radiated power of the heatsink. The predicted result agrees well with the measurement results. This study demonstrates possibility of an effective combination of near field scanning systems with numerical modeling tools for practical EMC investigations.

1.6. CONCLUSION & FUTURE WORK

In this section, the emission source microscopy (ESM) methodology has been introduced and performed to identify the sources of the radiation on different DUTs. In the theory part of this thesis, two different wave diffraction descriptions have been introduced which can be applied for the near-field and far-field diffraction respectively. Then the angular spectrum method is used for modeling the propagation of a wave field. This is the fundamental part of the ESM method. The resolution of the diffraction-limited system has also been discussed to improve the resolution of the ESM system. After that, the ESM method has been performed on two different DUTs at high frequency and low frequency respectively to evaluate the performance of the source identification of the method. Furthermore, the NF to FF transformation techniques has also been performed on the heatsink radiation prediction and the predicted result agrees well with the measurement.

In the future work of this project, it will be focused on how to improve the resolution of the ESM methodology. From the results of the computer screen testing, it can be seen that the resolution of the reconstructed data at 1.5GHz is around 20 cm by 20 cm. The resolution of the reconstructed data is strongly dependent on the refractive index of wave-travelling medium. Changing the wave-travelling medium to water, which has

the refractive index of 9 at 1 GHz, will significantly improve the resolution of the reconstructed field. However, the signal loss should be also considered when it is travelling from the water. This part of work is under processing and it will be shown in later publications.

2. DESIGNING A 3D PRINTING-BASED CHANNEL EMULATOR WITH PRINTABLE ELECTROMAGNETIC MATERIALS

2.1. ABSTRACT

This paper explored the possibility of building channel emulators by utilizing fused deposition modeling (FDM) 3D printing technology. The FDM 3D printing provides a rapid and economic method to produce parts with different shapes. Parts with different dielectric constants and loss tangents can be printed. Those parts will be placed or directly printed on a low loss transmission line to modify its transmission or reflection. An optimizing algorithm was developed for obtaining a printing pattern that leads to a desired loss profile. As a result, different channel emulators can be built to emulate the S-parameter and eye diagrams of a target channel with the advantage of avoiding complicated electronic components, and only being limited in the frequency range by the transmission line and attached connectors.

2.2. INTRODUCTION

Digital signals with fast rising/falling edges may be distorted by reflections, crosstalk, losses, and dispersive materials, causing signal integrity (SI) issues in a channel [36]-[39]. These SI issues need to be investigated carefully to meet ever tighter design constraints. Channel emulators are often used to evaluate communication system performance either in absence of the real channel or to test the system's response for varying channel characteristics. Available emulation approaches can be divided into simulation and hardware solutions. Simulation-based methods are usually applied to some simple channel emulation due to the software-based models limitation.

To perform a test in hardware, one is required to manufacture a vehicle for testing a design concept. This hinders progress in the design of high speed data links. A channel

emulator instrument can overcome this limitation partially. This instrument adjusts the properties of its channel to match a set of desired S-parameters. After connecting the drivers and receivers to channel emulator instrument, the SI performance of the channel can be evaluated either using eye diagrams or bit error rates. The simplest channel emulators are made of switchable fixed cables [40]. However, this gives very little flexibility because of the limited number of channel models. Another approach is using real-time digital signal processing (DSP) [41]. The DSPs are used to realize the S-parameters to create the output signal from the input signal. However, this approach is not feasible at a reasonable cost for high data rates.

To overcome the disadvantages of the previous two channel emulator methods, 3D printing based channel emulator was proposed. The 3D printing technology has been found growing applications in RF areas, such as horn antenna [42], coplanar waveguide [43][44] and electronic circuit [45][46]. Recently, people have printed a spatially variant anisotropic metamaterial with the low loss printable material [47][48]. This kind of metamaterial can be used to sculpt the near field around devices. A typical 3D printer can print structures with high resolution, different geometries and various densities, which may be expensive, or impossible to be made by conventional machining methods.

Considering the high flexibility of 3D printing technology, the concept of using FDM 3D printing to create channel emulators was proposed. By placing 3D printable electromagnetic materials on a low loss transmission line, the electromagnetic behavior of a channel will be modified. With suitable material patterns, a target channel can be emulated. Avoiding electronics is the major advantage of a 3D printing-based channel emulator. This will lead to a robust, economical solution for high-speed SI problems.

Extended from a previous paper [49], this paper [50] explains the 3D printing based channel emulator method and the material property of high dielectric constant materials and electrically or magnetically lossy materials. The emulated channel with 3D printed method is compared against the target channel in terms of simulated eye diagrams at different data transfer rates.

2.3. LOW LOSS TRANSMISSION LINE DESIGN

Fig. 2.1 shows a 2-layer 50 Ω microstrip trace as a base for overlaying the 3D printable materials. Its substrate is made from Megtron 6 with the relative dielectric constant of 3.6 [51]. The board is 20 mil thick and 18,000 mil long. There is a 38 mil wide slot on the bottom ground layer. The field will leak from the slot and may interact with materials placed on the bottom and at the top. In this way, it enables us to emulate the channel by placing the materials both on top and bottom of the microstrip.

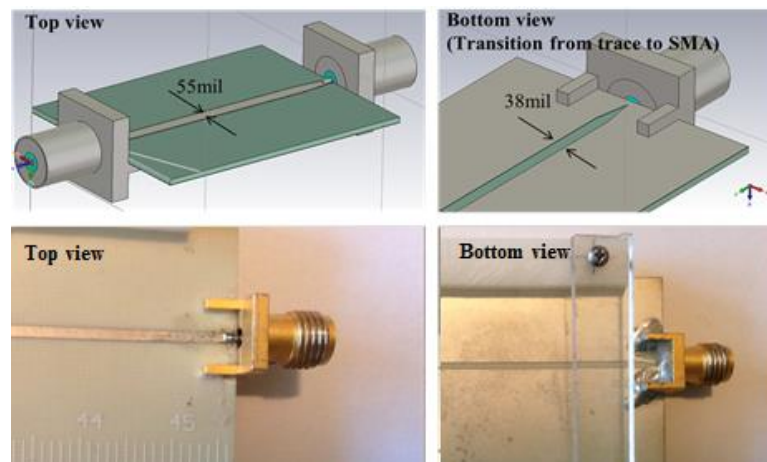


Figure 2.1. Full-wave CST [52] model and pictures of low loss microstrip trace. The length of the full-wave model was scaled down for illustration purpose.

The measured and simulated transmission coefficients S_{21} are shown in Fig. 2.2 with minor mismatch (<0.5 dB) below 12 GHz. This is due to the mismatch between the material parameters in CST and the real one used in the board. In spite of the minor mismatch, the S_{21} can still be considered to be linear up to 25 GHz, which is important for creating 3D printing-based channel emulators.

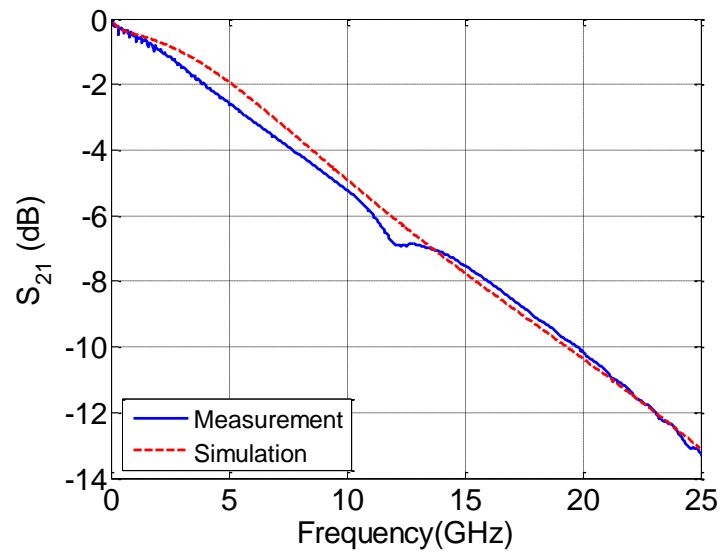


Figure 2.2. Comparison of measured and simulated transmission coefficients S_{21} of the low loss microstrip trace.

2.4. DEVELOPMENT OF 3D PRINTING FILAMENT WITH HIGH DIELECTRIC CONSTANTS AND LOSS PROPERTY

Acrylonitrile butadiene styrene and polylactic acid with low dielectric constant are widely used as 3D printing materials [53]. However, materials with high dielectric constant and loss property are needed for channel emulation application. The Maxwell Garnett rule in [54] can help to determine mixing ratios and predict dielectric constants. The mixed material then can be extruded as filament for 3D printing.

2.4.1. Printable High Dielectric Constant Materials. TiO₂ was used as a filler to be mixed with a proprietary base polymer, considering its high permittivity in the Radio Frequency (RF) range. The ratio of TiO₂ to the base polymers determines the hardness, flow rate and tensile strength of the filament, such that the filament can be printed without being broken if the fill ratio is not too high. Based on this consideration, three different weight percentages (70%, 74% and 76%) of TiO₂ were manufactured and investigated for their RF and printing properties.

To print these filaments, there are certain conditions that need to be satisfied [55]. The temperature setting of the printer nozzle is an important factor to print a good structure. If the temperature is too high, the material will melt too early and leak out from the extruder while moving in separate areas of the print. If the temperature is too low, the filament will not stick together or even not print out. The melting points of the filaments are related with the mixing percentages of TiO₂. To obtain optimal results for the printing, variables like the diameter of 3D printer nozzle, the printing speed, and layer height need to be taken into account. Table 2.1 shows the optimized printer settings for the materials different weight percentages (70%, 74% and 76%) of TiO₂.

Table 2.1 Optimized printer settings for the different materials

Material name	Extruder Temp.	Bed Temp.	Layer height	Printing speed	Extrusion width
Mars (70% TiO ₂)	140 °C	Non	0.25 mm	16 mm/s	0.6 mm
Caldera (74% TiO ₂)	180 °C	60 °C	0.25 mm	16 mm/s	0.6 mm
Valcanus (76% TiO ₂)	220 °C	60 °C	0.25 mm	16 mm/s	0.6 mm

In 3D printing, the infill pattern and material density can be adjusted. Slic3r [56] is used as slicing software, which offers several infill patterns at varying infill densities, such as: honeycomb, concentric, line, etc. By adjusting the 3D printing parameters, materials with different effective permittivity can be obtained. A more complex pattern will require more time [57] to print. In the channel emulator application, solid printing is desired to achieve the highest dielectric constant and ensure the isotropic material prosperities of the printed block. Table 2.2 shows the density comparison of the raw material and the printed blocks, which are calculated based on the weight and volume of the materials. From the comparison, it can be seen that the density of the printed blocks are very close to the raw material density. Thus, with the appropriate setting of the printer, 100% solid printing can be achieved.

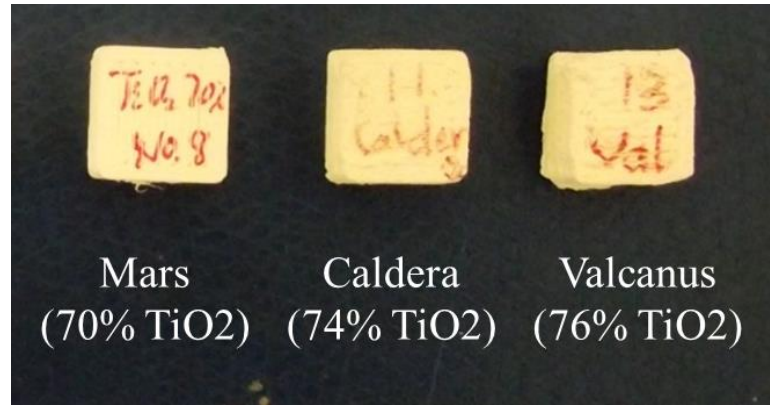
Table 2.2 Material density comparison

Material name	Raw material density	Printed block density
Mars (70% TiO ₂)	1.87 (1.84 – 1.93)	1.99 (1.96 – 2.01)
Caldera (74% TiO ₂)	1.83 (1.76 – 1.89)	1.95 (1.90 – 2.00)
Valcanus (76% TiO ₂)	1.97 (1.80 – 2.23)	1.98 (1.92 – 2.05)

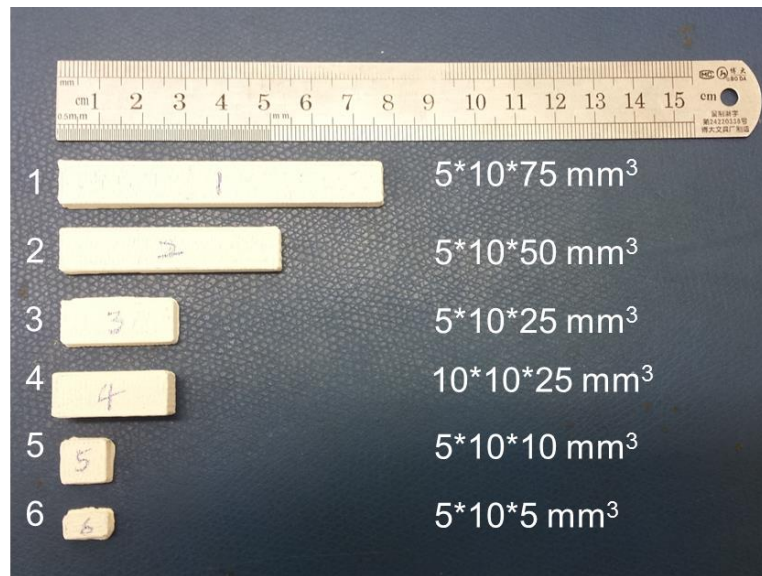
The number outside of the bracket are the average values of the density.

The number inside the bracket are the varying ranges of the density.

Fig. 2.3 (a) shows several printed blocks with different mixing ratios of TiO₂. The blocks are solid, with the sizes of 1 cm × 1 cm × 0.5 cm. Fig. 3 (b) shows several printed Caldera blocks with different sizes.



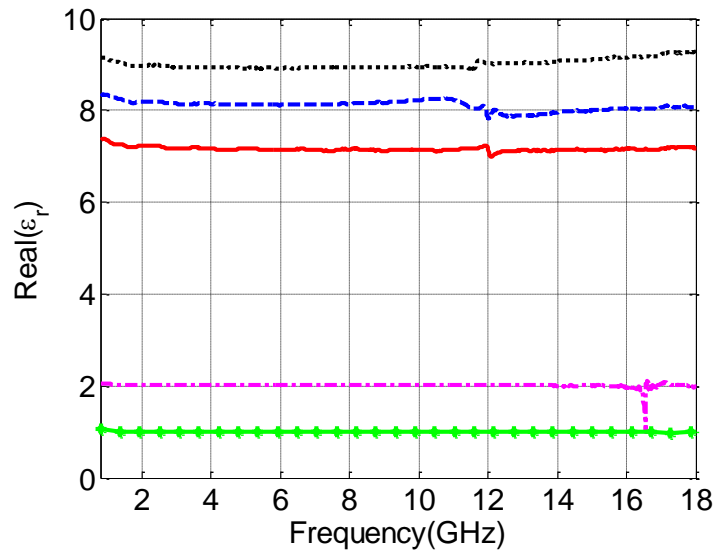
(a)



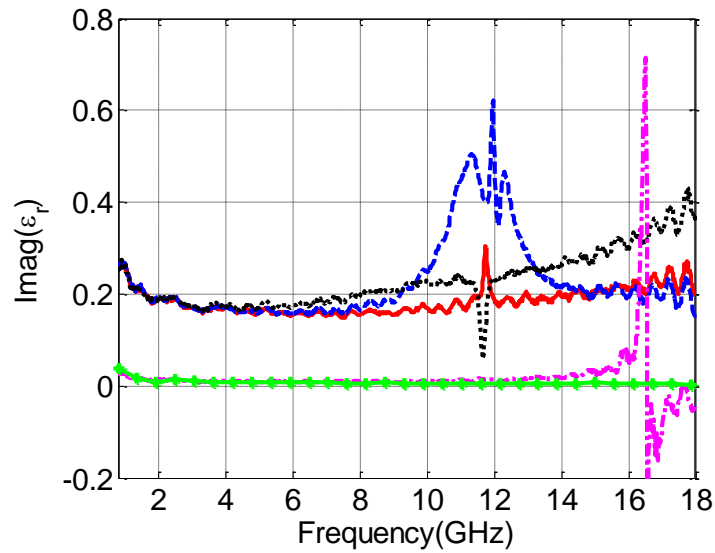
(b)

Figure 2.3. Printed blocks with different mixing ratios of TiO₂ (a) and different sizes (b).

The dielectric properties of printed materials were characterized from 800 MHz to 18 GHz using 7/3 mm coaxial airline method [58]. Fig. 2.4 shows the real part (a) and imaginary part (b) of measured permittivity of the high permittivity materials shown in Fig. 2.3 (a). Air ($\epsilon_r = 1$) and Teflon ($\epsilon_r = 2$) have also been measured to test the measurement accuracy.



(a)



(b)

Figure 2.4. The real part (a) and imaginary part (b) of measured permittivity of different TiO_2 ratio mixed high permittivity materials. Air and Teflon are also plotted for comparison.

It shows that the permittivity of the printed material is constant up to 18 GHz.

While increasing the weight percentage of TiO_2 , the real part of permittivity of the mixed

materials will also increase. For the 76% TiO₂ material, the dielectric constant is about 9. If a lower dielectric constant is desired, the density of the 3D printed material can be adjusted. The imaginary part of the permittivity of the mixed materials is around 0.2 and keeps constant up to 18 GHz. Since TiO₂ has very low loss in the GHz region ($\epsilon_r'' = 6.2 \times 10^{-3}$ around 3 GHz [59][60]), the material loss might be from the dielectric base materials and the measurement uncertainty. The observed resonances around 12 GHz for high permittivity materials are most likely due to the resonance associated with the standing wave within the thickness of the test washers [58]. By adding the high permittivity material on the top of the trace, the characteristic impedance of the channel can be changed. For instance, the characteristic impedance of the trace can be reduced from 55.61 Ohm to 47.9 Ohm, by adding 74% TiO₂ mixed material. Based on this conclusion, periodic structure can be used to produce resonance dip to the channel's frequency response. This periodic structure will be discussed in Section 2.5 and Section 2.6.

2.4.2. Printable Electrically Lossy Materials. To match with the loss function of a target S-parameter, lossy material blocks with different sizes can be placed or printed directly on the trace. The “carbomorph” [45], which is made by adding carbon black filler to a matrix of polycaprolactone, is an electrically lossy material. This material can provide a smooth linear loss up to 25 GHz. The printing temperature of carbomorph is 240 °C.

Fig. 2.5 shows a carbomorph block with dimensions of 3.3 cm by 1.1 cm. This carbomorph block can be placed on the top of the trace in two orientations. Fig. 2.5 compares the S_{21} parameters of the channel with different lengths of carbomorph blocks

placed on the trace. For a target channel with linear loss, one can simply place the lossy material block with suitable length on the trace to achieve a desired loss profile. This can also be used to emulate the loss behavior of long channels by using a short channel with lossy materials [61].

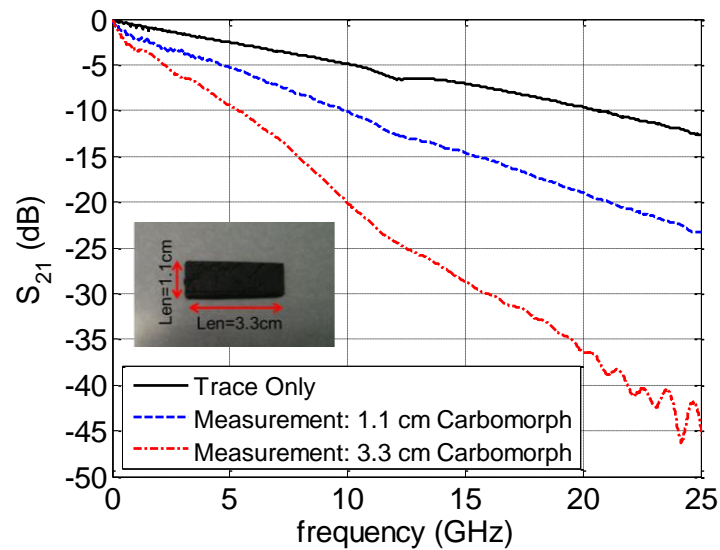


Figure 2.5. Comparison of S_{21} parameters with different lengths of carbomorph blocks placed on the trace.

Another electrically lossy material, called carbonara [45], was mixed using another base polymer. It was extruded as filament for 3D printing. The printing temperature of carbonara is 150 °C. Fig. 2.6 shows the measured dielectric constant of the carbonara filament using 7/3 mm coaxial airline method [58]. The measured carbonara material parameters are imported into CST for the Debye model fitting. In CST, the material property is defined based on a Debye dispersion model, which requires user to input the electric tangent delta value given at the defined frequency and the model order [52]. CST performs complex fitting in the Debye complex conjugate terms, with poles

fulfilling passivity. This automatically complies with Kramers-Krönig relationships [62]. The CST fitted data can be used to describe the material property. Fig. 2.6 compares the measured material parameters and curve-fitted data from the CST. For the carbonara material definition in CST, the third order Debye model is used, the real part of permittivity is defined as 6.3, and the electric loss tangent is defined as 0.095 at 4 GHz.

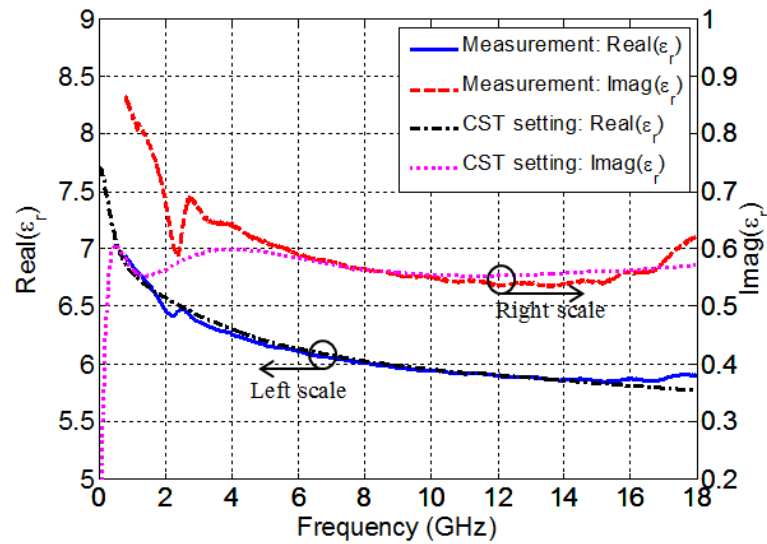


Figure 2.6. The comparison of measured Carbonara material parameters with the CST setting.

To validate the measured material properties and its curve fitting, a block of lossy material was printed on a trace. The S_{21} parameters were measured and compared with the results of the simulation model. The carbonara block size was $1.0 \text{ cm} \times 1.0 \text{ cm} \times 0.2 \text{ cm}$. Similar blocks have been printed multiple times to test the repeatability of the printing. The printed block was arbitrarily placed on the top of the trace without choosing any special location along the trace. Based on the trace model and the printed block information, the CST model of the microstrip trace with block was built up to confirm the

validity of the measured and curve-fitted material properties. In the CST material setting, the Debye model curve-fitted data are used for the carbonara material parameters. Fig. 2.7 compares the S_{21} parameter between measurement and simulation. The deviation is less than 1dB and the general loss vs. frequency increase is well matched.

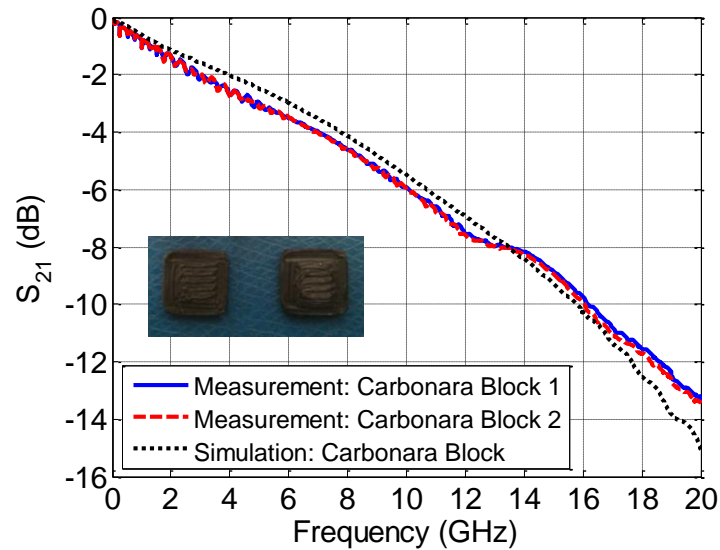
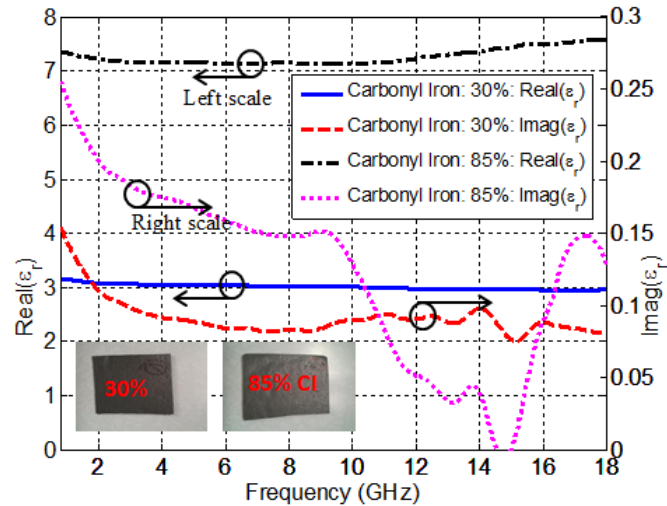


Figure 2.7. Measured and simulated S_{21} parameters comparison using a 1 cm by 1 cm by 0.2 cm carbonara block on the trace.

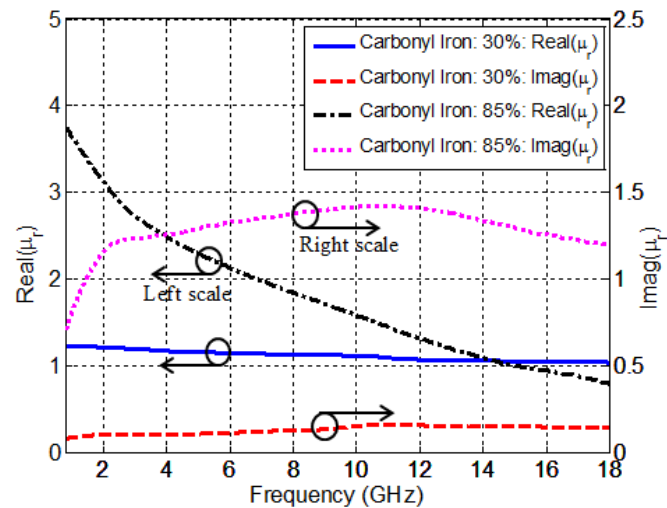
2.4.3. Printable Magnetically Lossy Materials. Magnetically lossy materials were printed using a filament made of a polymer filled with different weight percentages of carbonyl iron (CI). Fig. 2.8 (a) shows two samples of magnetically lossy material with different CI weight ratios.

The measured material parameters are also shown in Fig. 2.8. With carbonyl iron added, the mixed material has comparatively higher complex permittivity. From Fig. 2.8 (a), it can be seen that the real part of permittivity of the 85% carbonyl iron sample is about 7.2. This high permittivity property will also affect the characteristic impedance of

the emulated channel. For the permeability of the CI mixed materials, as shown in Fig. 2.8 (b), the real part decreases with the frequency, while the imaginary part reaches a maximum around 10 GHz. This shows the typical magnetically lossy material property, matching with literature data [63].



(a)



(b)

Figure 2.8. The measured complex permittivity (a) and permeability (b) of two magnetically lossy materials with 30% and 85% CI weight ratios.

To study the capability of the magnetically lossy materials for channel emulation, three blocks with different CI weight ratios were placed on the top of the base trace and then S_{21} parameters were measured for each block. Attenuation coefficient, which expresses the unit length loss of the trace, is compared to study the magnetically lossy material property, as shown in Fig. 2.9. The 75% CI mixed lossy material provides the best compromise between smooth loss increase and high loss over the frequency of interest.

In Fig. 2.10, the attenuation coefficients of the magnetically (Carbonyl Iron) and electrically (Carbonmorph) lossy materials are compared to show different frequency dependencies. The attenuation constant of the carbomorph is proportional to the angular frequency, while the attenuation constant of the carbonyl iron is dominated by dependence. This frequency dependence helps select the appropriate lossy material for emulating the loss of target channels [61].

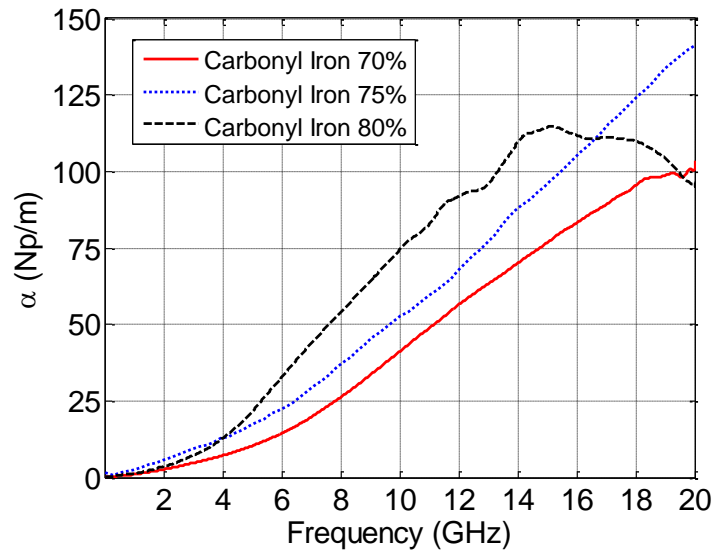


Figure 2.9. Attenuation coefficient α comparison of raw magnetically lossy material with different CI weight ratios.

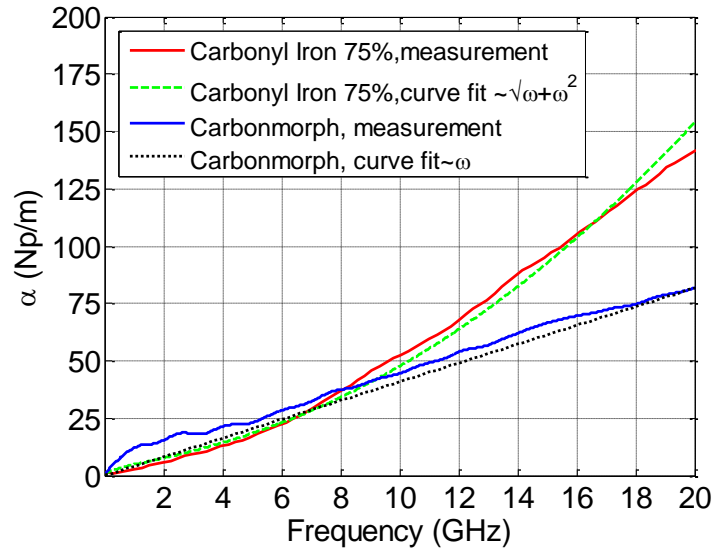


Figure 2.10. Comparison of the attenuation coefficients of electrically (Carbonyl Iron) and magnetically (Carbonmorph) lossy materials.

2.5. DETERMINE 3D PRINTING PROFILE FOR A CHANNEL EMULATOR

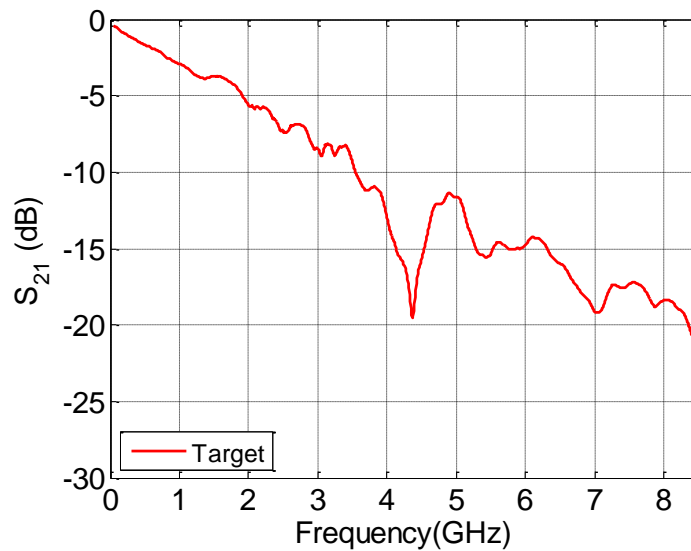


Figure 2.11. A typical S_{21} parameter target function from 100 kHz to 8.5 GHz.

The nonideal effects of a channel are closely related to the geometrical features and material properties. Here channel loss is the property of greatest interest. Typically, the channel loss is characterized by the following two parts: a smooth roll-off of amplitude with frequency, and dips in the magnitude response caused by reflections or radiations. Fig. 11 shows the S_{21} parameter of a typical channel from 100 kHz to 8.5 GHz. This target S_{21} parameter showed a loss increase of about 5 dB every 2 GHz and a dip caused by reflections or radiation at about 4.3 GHz.

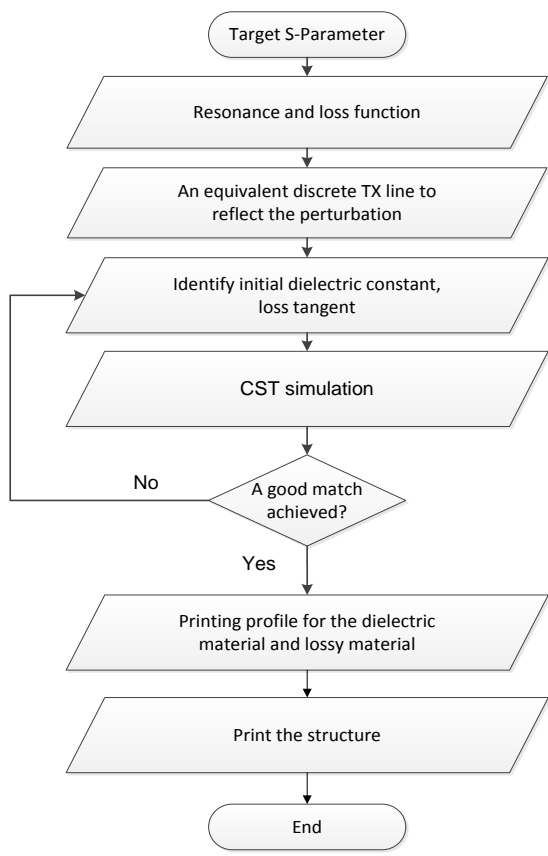


Figure 2.12. Flow chart for determining the printing profile for the channel emulator.

In the 3D printed channel emulator, an algorithm is developed for obtaining the best matching printing pattern. Fig. 2.12 shows the flow chart for determining the material printing profile. Initially, a target channel described by S-parameters is needed. This is used to identify an equivalent transmission line described by the resonance and a smooth loss. These continuous dependencies, in turn, can be approximated with discrete sequences, producing a discrete transmission line (or a layered medium). This will reflect the real perturbation of an ideal transmission line found in a real system.

The printed periodic high dielectric constant blocks can be used to simulate the frequency-dependent null on the S-parameters. And by adding lossy material, the smooth loss of the target can be approximately emulated. In this project, CST Microwave Studio optimization function is utilized to find an equivalent channel.

The initial value of the period parameters to be optimized can be set according to the fiber Bragg grating theory [64]. Supposing there is a resonance of interest at f_0 , the relative permittivity of the printing material is ϵ_r , the period length of the structure is T , and the length of each material block along the trace direction is a . The relation between these parameters is given by Eq. 2.1 [65]:

$$a \times \sqrt{\epsilon_r} + (T - a) = \frac{c}{2f_0} \quad (2.1)$$

Here, c is the speed of light in the vacuum. So the initial value of T and a can be determined. Then, the transient solver of the optimizer in CST can be used to further optimize the transmission line's parameters, such as the period and size of the blocks.

After a good match between the simulation and the target S-parameter achieved, the printing profile including the geometric information and the dielectric constants of the printed parts, can be obtained.

2.6. TEST CASES

Using the channel depicted in Fig. 2.11 as a target channel, a test case is shown for demonstrating the procedure of designing a 3D printing-based channel emulator. Based on the resonance frequency of target channel and the measured high permittivity material parameters, initial periodic blocks structure can be approximately calculated from Eq. (1). Then 3D optimization with higher weight factor on the interested parts of the target can be conducted using CST microwave studio. In this simulation, the high permittivity material parameters setting is according to the coaxial airline measurement result, with the real part of the permittivity to be 8.4, and the loss tangent to be 0.02. The period, size and number of the high permittivity material blocks can be optimized in the simulation to obtain a good match with the resonant frequency and depth of the S_{21} dip in the target channel. The lossy material parameters used in the simulation are the CST fitted data of the carbonara material. The length of the lossy material blocks can also be optimized in the simulation to match with the insertion loss of the target channel.

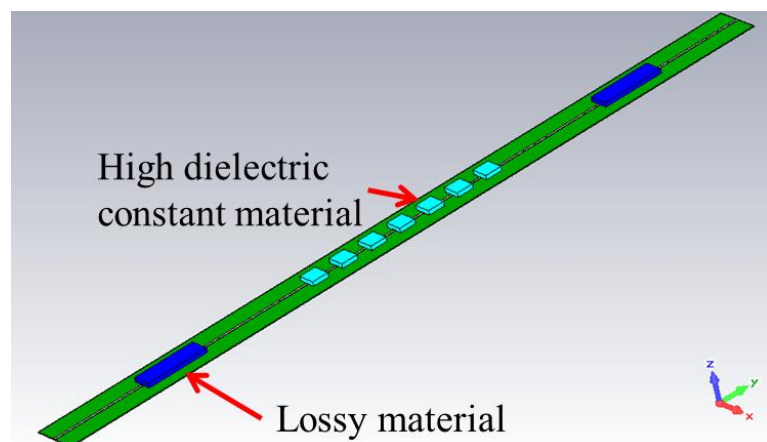


Figure 2.13. Printing pattern on the simulated channel.

Fig. 2.13 shows the transmission line with the optimized periodic high dielectric constant blocks placed on the top side. The period of the blocks is 760 mils and the sizes of these blocks are 400 mil \times 400 mil \times 100 mil. The length of the lossy material blocks is optimized to be 5800 mil to match with the target insertion loss.

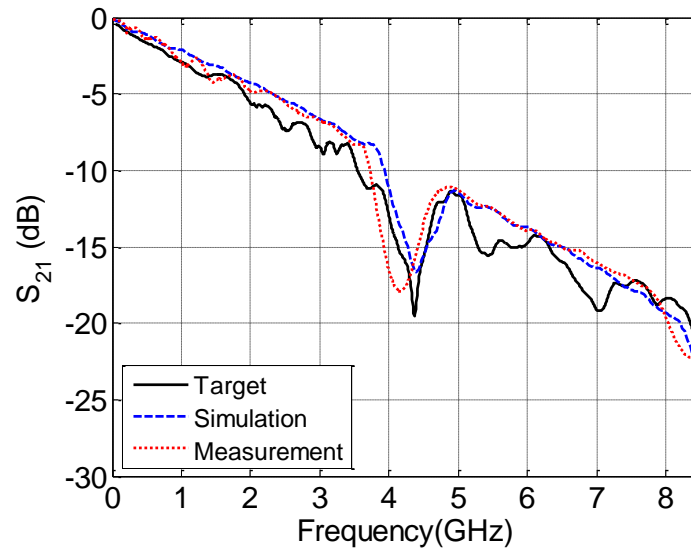


Figure 2.14. S_{21} comparison of the target channel, simulation and measurement results.

Fig. 2.14 compares the target and simulated S_{21} parameters. The dip of the simulated S_{21} matches well with the target. And the frequency dependent loss of the simulated S_{21} also matches with the target channel approximately.

After obtained the optimized periodic blocks parameters, this information can be translated into a printing profile, including the geometry and pattern information of the blocks. As shown in Fig. 2.15, the periodic blocks can be directly printed on the trace. Here, the printing material contains 70% TiO_2 . The carbonara blocks are prepared with a suitable length to match the smooth roll-off of amplitude with frequency on this target.

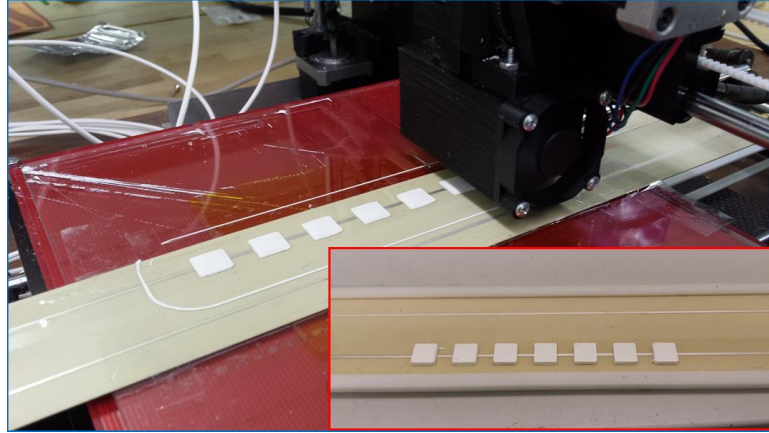


Figure 2.15. Printing high dielectric constant material blocks on the trace.

The measured S_{21} of the trace with the periodic blocks has been compared with the target, shown in Fig. 2.14. The resonance dip of the S_{21} is clearly shown in the measurement, which is caused by the printed periodic structure on the trace. This dip frequency has a small mismatch with the target, and it might be caused by the printing precision of the printer or a deviation of the printed dielectric constant. This mismatch can be corrected by slightly tuning the size of the blocks. Furthermore, in this measurement, the smooth roll-off of amplitude of the S_{21} is matched well with the target.

In the S_{21} comparison, the phase information is not shown, since it is not used as a goal criterion in the optimization. However, eye diagrams of the emulated channel are used to evaluate the channel performance. The eye diagram of the channel is sensitive to the dispersive phase of the S_{21} parameter (the linear phase term just acts as a delay). The good match of the eye diagrams indicate that the relevant dispersive phase terms are also matched, although they have not been directly used to formulate the goal function of the optimization.

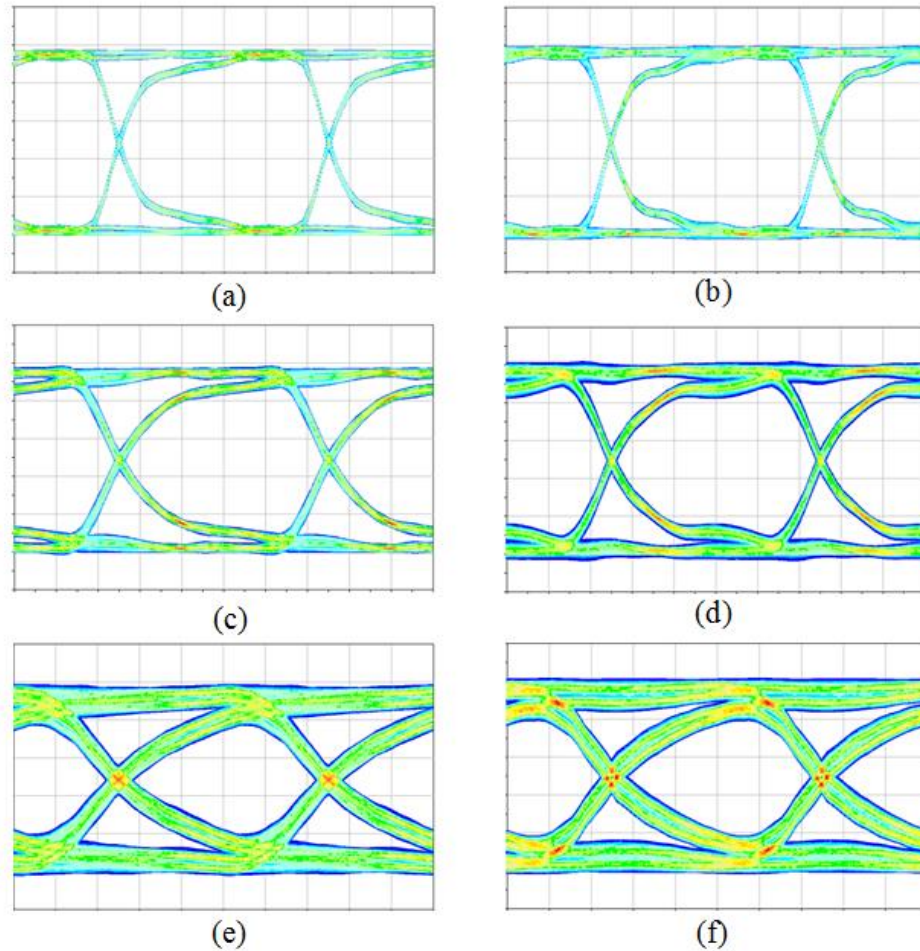


Figure 2.16. Comparison of eye diagrams from the target and the emulated channel. (a), (c) and (e) are the eye diagrams of the target with 1 Gbps, 2 Gbps and 4 Gbps bit rate, respectively. (b), (d) and (f) are the eye diagrams of the emulated channel with 1 Gbps, 2 Gbps and 4 Gbps bit rate, respectively.

In Fig. 2.16, the eye diagrams obtained from the target and the emulated channel are compared. Three different data rates which are 1 Gbps, 2 Gbps and 4 Gbps, respectively, are simulated for the comparison. The rise and fall time of the signal is fixed with 5% of the periods, which are 100 ps, 50 ps and 25 ps, correspondingly. Table II also compares the JitterPP, height and width of the eye diagram between the target and the emulated channel. It can be clearly seen that 3D printing emulated channel is comparable with the target channel.

Table 2.3 Eye diagram parameters comparison.

Bit Rate	Channel	JitterPP	Height	Width
1 Gps	Target	10 ps	0.389 V	990 ps
	Emulated	10 ps	0.419 V	990 ps
2 Gps	Target	20 ps	0.333 V	480 ps
	Emulated	17.5 ps	0.336 V	482 ps
4 Gps	Target	312 ps	0.213 V	219 ps
	Emulated	312 ps	0.234 V	219 ps

2.7. CONCLUSIONS

This section shows that channel emulators can be created by utilizing FDM 3D printing technology. Printable high dielectric constant and lossy materials are developed. With a target channel, both smooth roll-off loss and resonance dip can be achieved by printing the suitable material block pattern on a low loss trace. A 3D printed channel has been created and measured. The measured S-parameter of the channel emulator matches well with the target channel. It is demonstrated that this method is efficient and economical to create channel emulators. Furthermore, 3D printing of dielectric, electrically and magnetically lossy materials may enable electromagnetic compatibility (EMC) and SI correction overlays, compensation structures for shielding and field guiding, printed antenna arrays, and cross talk emulation.

BIBLIOGRAPHY

- [1] A. D. Yaghjian, "An overview of near-field antenna measurements," *IEEE Transactions on Antennas and Propagation*, vol. 34, no. 1, pp. 30-45, 1986.
- [2] X. Jiao, P. Maheshwari, V. Khikevich, P. Dixon, Y. Arien, A. Bhohe, J. Li, X. Li, D. Pommerenke, J. Drewniak, H. Kajbaf, J. Min, "EMI mitigation with lossy material at 10 GHz," *Electromagnetic Compatibility (EMC), 2014 IEEE International Symposium on*, pp. 150-154, Aug. 2014.
- [3] Q. Liu, X. Jiao, J. Li, V. Khilkevich, J. Drewniak, P. Dixon, Y. Arien, "Modeling absorbing materials for EMI mitigation," *Electromagnetic Compatibility (EMC), 2015 IEEE International Symposium on*, pp. 1548-1552, Aug. 2015.
- [4] A. Bhohe, H. Chu, L. Comiskey, X. Jiao, X. Li, "Thermal and EMI Performance of Composite Plastic Molded Heat Sinks and Hybrid TIM Materials," *2014 International Symposium on Microelectronics*, vol. 2014, no. 1, pp. 000222-000228, FALL 2014.
- [5] M. Koledintseva, K. N. Rozanov, and J. L. Drewniak, "Engineering, modeling and testing of composite absorbing materials for EMC applications", in *Advances in Composite Materials - Ecodesign and Analysis*, ed. B. Attaf, InTech, Ch. 13, pp. 291-316, Mar. 2011.
- [6] J. Li, X. Li, S. Toor, H. Fan, A. U. Bhohe, J. Fan, J. L. Drewniak, "EMI Coupling Paths and Mitigation in a Board-to-Board Connector," in *Electromagnetic Compatibility, IEEE Transactions on*, vol. 57, no. 4, pp. 771-779, Aug. 2015.
- [7] P. L. Ransom, and R. Mitra, "A method of locating defective elements in large phased arrays," *Proc. of the IEEE*, vol. 59, no. 6, pp. 1029-1030, 1971.
- [8] M. Fallahpour, M. Ghasr, J.T. Case, and R. Zoughi, "A Wiener Filter-Based Synthetic Aperture Radar (SAR) Algorithm for Microwave Imaging of Targets in Layered Media", *Materials Evaluation*, vol. 69, no. 10, pp. 1227-1237, Oct. 2011.
- [9] D. M. Sheen, D. L. McMakin, and T. E. Hall, "Three-dimensional Millimeter-Wave Imaging for concealed Weapon Detection," in *IEEE Transactions on Microwave Theory and Techniques*, vol. 49, no. 9, pp. 1581-1592, 2001.
- [10] Z. Yang, Y. R. Zheng, "Near-field 3-D synthetic aperture radar imaging via compressed sensing," in *Acoustics, Speech and Signal Processing (ICASSP), 2012 IEEE International Conference on*, pp. 2513-2516, 25-30 March 2012.
- [11] Z. Yang, Y. R. Zheng, "A comparative study of compressed sensing approaches for 3-D synthetic aperture radar image reconstruction," *Digital Signal Processing*, vol. 32, pp. 24-33, September 2014.

- [12] H. Kajbaf, J. T. Case, Z. Yang, Y. R. Zheng, “Compressed sensing for SAR-based wideband three-dimensional microwave imaging system using non-uniform fast Fourier transform,” *Radar, Sonar & Navigation, IET*, vol. 7, no. 6, pp. 658-670, July 2013.
- [13] D. A. B. Miller, “Huygens’s wave propagation principle corrected,” *Opt. Lett.* vol. 16, pp. 1370–1372, 1991.
- [14] Wikipedia, “Huygens–Fresnel principle,” [Online]. Available: https://en.wikipedia.org/wiki/Huygens%E2%80%93Fresnel_principle#cite_note-1.
- [15] M. K. Kim, *Digital Holographic Microscopy Principles, Techniques, and Applications*, Springer-Verlag, New York, 2011.
- [16] J. W. Goodman, *Introduction to Fourier Optics*, Roberts and Company Publishers, 2004.
- [17] Wikipedia, “Fresnel diffraction,” [Online]. Available: https://en.wikipedia.org/wiki/Fresnel_diffraction.
- [18] Wikipedia, “Fraunhofer diffraction,” [Online]. Available: https://en.wikipedia.org/wiki/Fraunhofer_diffraction.
- [19] G. C. Sherman, “Application of Convolution Theorem to Rayleighs Integral Formulas,” *Journal of the Optical Society of America*, vol. 57, pp. 546–547, 1967.
- [20] J. T. Case, M. T. Ghasr, and R. Zoughi, “Optimum Two-Dimensional uniform spatial sampling for microwave SAR-Based NDE imaging,” *IEEE Transactions on Instrumentation and Measurement*, vol. 60, no. 12, pp. 3806-3815, 2011.
- [21] Wikipedia, “Diffraction-limited system,” [Online]. Available: https://en.wikipedia.org/wiki/Diffraction-limited_system.
- [22] G. Muchaidze, J. Koo, Q. Cai, T. Li, L. Han, A. Martwick, K. Wang, J. Min, J. L. Drewniak, and D. Pommerenke, “Susceptibility Scanning as a Failure Analysis Tool for System-Level Electrostatic Discharge (ESD) Problems,” *IEEE Transactions on Electromagnetic Compatibility*, vol. 50, no. 2, pp.268-276, 2008.
- [23] K. Wang; D. Pommerenke, J. M. Zhang, and R. Chundru, “The PCB level ESD immunity study by using 3 dimension ESD scan system,” *International Symposium on Electromagnetic Compatibility*, vol. 2, pp.343-348, 2004.

- [24] M. Abramowitz and M. W. Davidson, "Microscope Objectives: Numerical aperture and resolution," *Molecular Expressions: Optical Microscopy Primer (website)*, Florida State University, April, 2004.
- [25] M. Saitoh, T. Yamamoto, T. Sakamoto, H. Niori, M. Chino, and M. Kobayasi, "Electromagnetic wave absorber using dielectric (Ti)-magnetic(Fe) composite material for GHz frequency band," *Proceedings of the 12th IEEE International Symposium on Applications of Ferroelectrics*, vol. 2, pp. 871-874, 2000.
- [26] Laird Technologies, "Microwave Absorber: ECCOSORB," [Online]. Available: <http://www.eccosorb.com/products-eccosorb-bsr.htm>.
- [27] G. Koepke and J. Ladbury, "Radiated Power Measurements in Reverberation Chambers," *56th ARFTG Conference Digest-Fall*, vol. 38, pp.1-7, 2000.
- [28] W. Huang, D. Pommerenke, X. Jiang, D. Liu, M. Jin, G. Muchaidze, K. Soonjae, and H. K. Ki, "A measurement technique for ESD current spreading on a PCB using near field scanning," *IEEE 2009 International Symposium on Electromagnetic Compatibility*, pp. 18-23, Aug. 2009.
- [29] C. E. Brench, "Heatsink Radiation as a Function of Geometry", *IEEE International Symposium on EMC*, pp105-109, Aug 1994.
- [30] C. Wang, J. L. Drewniak, J. L. Knighten, D. Wang, R. Alexander, D. M. Hockanson, "Grounding of heatpipe/heatspreader and heatsink structures for EMI mitigation", *2001 IEEE EMC International Symposium on EMC*, pp 916 – 920, 2001.
- [31] J. Zhang, K. Kam, J. Min, V. Khilkevich, D. Pommerenke and J. Fan, "An Effective Method of Probe-calibration in Phase Resolved Near-field Scanning for EMI Application," *IEEE Transactions on Instrumentation & Measurement*, vol. 62, no. 3, pp. 648-658, March 2013.
- [32] A. Radchenko, J. Zhang, K. Kam; D. Pommerenke, "Numerical evaluation of Near-Field to Far-Field transformation robustness for EMC," *2012 IEEE International Symposium in Electromagnetic Compatibility (EMC)*, pp.605-611, 6-10 Aug. 2012.
- [33] G. Koepke and J. Ladbury, "Radiated Power Measurements in Reverberation Chambers," *56th ARFTG Conference Digest-Fall*, vol. 38, pp. 1-7, 2000.
- [34] C. L. Holloway, D. A. Hill, M. Sandroni, J. M. Ladbury, J. Coder, G. Koepke, A. C. Marvin, Y. He, "Use of Reverberation Chambers to Determine the Shielding Effectiveness of Physically Small, Electrically Large Enclosures and Cavities," *IEEE Transactions on Electromagnetic Compatibility*, vol.50, no.4, pp.770-782, Nov. 2008.

- [35] O. M. Bucci, G. D'Elia, G. Leone, R. Pierri, "Far-field pattern determination from the near-field amplitude on two surfaces", *IEEE Transactions on Antennas and Propagation*, vol. 38, no. 11, pp. 1772-1779, 1990.
- [36] J. J. Olmos, A. Gelonch, F. J. Casadevall, G. Femenias, "Design and implementation of a wide-band real-time mobile channel emulator," *IEEE Trans. on Veh. Technol.*, vol. 48, no. 3, pp. 746-764, 1999.
- [37] H. Eslami, S. V. Tran, A. M. Eltawil, "Design and Implementation of a Scalable Channel Emulator for Wideband MIMO Systems," *IEEE Trans. on Veh. Technol.*, vol. 58, no. 9, pp. 4698-4709, 2009.
- [38] J. Zhang, J. Lim, W. Yao, K. Qiu, R. Brooks, "PCB Via to Trace Return Loss Optimization for >25Gbps Serial Links," *IEEE Int. Symp. Electromag. Compat.*, August 3-8, 2014.
- [39] S. Jin, J. Zhang, J. Fan, "Optimization of the transition from connector to PCB board," *IEEE Int. Symp. Electromag. Compat.*, pp. 192-196, August 5-9, 2013.
- [40] Agilent, "Agilent M8048A ISI Channels Master Your Next Designs," [Online]. Available: <http://cp.literature.agilent.com/litweb/pdf/5991-3648EN.pdf>, 2014.
- [41] A. Patnaik, C. Ding, A. Talebzadeh, D. White, M. Tsiklauri, Stephen Scearce, D. Pommerenke, Y. Yang, "Implementation of a 18 GHz bandwidth Channel Emulator using an FIR filter", *IEEE Int. Symp. Electromag. Compat.*, pp. 950-955, 2014.
- [42] C. R. Garcia, R. C. Rumpf, H. H. Tsang, J. H. Barton, "Effects of extreme surface roughness on 3D printed horn antenna," *Electronics Letters*, vol. 49, pp. 734-736, 2013.
- [43] M. Ahmadloo, "Design and fabrication of geometrically complicated multiband microwave devices using a novel integrated 3D printing technique," *IEEE 22nd Conference on Electrical Performance of Electronic Packaging and Systems (EPEPS)*, pp. 29-32, Oct. 2013
- [44] E. A. Rojas-Nastrucci, T. Weller, V. L. Aida, F. Cai; J. Papapolymerou, "A study on 3D-printed coplanar waveguide with meshed and finite ground planes," *2014 IEEE 15th Annual Conference on Wireless and Microwave Technology (WAMICON)*, pp.1-3, 2014
- [45] S. J. Leigh, R. J. Bradley, C. P. Purssell, D. R. Billson, and D. A. Hutchins, "A Simple, Low-Cost Conductive Composite Material for 3D Printing of Electronic Sensors," *PLoS ONE*, vol. 7, no. 11, e49365, 2012.

- [46] Kenneth H. Church, Harvey Tsang, Ricardo Rodriguez, Paul Defembaugh, Raymond Rumpf. "Printed Circuit Structures, the Evolution of Printed Circuit Boards". IPC APEX EXPO Conference Proceedings, 2013.
- [47] C. R. Garcia, J. Correa, D. Espalin, J. H. Barton, R. C. Rumpf, R. Wicker, and V. Gonzalez, "3D printing of anisotropic metamaterials," *Progress In Electromagnetics Research Letters*, vol. 34, pp. 75-82, 2012.
- [48] R. C. Rumpf, C. R. Garcia, H. H. Tsang, J. E. Padilla, and M. D. Irwin, "Electromagnetic isolation of a microstrip by embedding in a spatially variant anisotropic metamaterial," *Progress In Electromagnetics Research*, vol. 142, pp. 243-260, 2013.
- [49] X. Jiao, H. He, G. Li, W. Qian, G. Shen, D. Pommerenke, C. Ding, D. White, S. Scearce, Y. Yang "Designing A 3D Printing-Based Channel Emulator," in *IEEE Int. Symp. Electromag. Compat.*, Raleigh, NC, 2014.
- [50] X. Jiao, H. He, W. Qian, G. Li, G. Shen, X. Li, C. Ding, D. White, S. Scearce, Y. Yang, D. Pommerenke, "Designing a 3-D Printing-Based Channel Emulator With Printable Electromagnetic Materials," *IEEE Trans. Electromagn. Compat.*, vol. 57, no. 4, pp. 868-876, Aug. 2015.
- [51] Gorilla Circuits, "Data sheet of Megtron 6," [Online]. Available: <http://www.gorillacircuits.com/documents/Data%20Sheets/Megtron6.pdf>, 2014.
- [52] Computer Simulation Technology AG, "CST STUDIO SUITE™," [Online]. Available: www.cst.com, 2014.
- [53] P. I. Deffenbaugh, R. C. Rumpf, K. H. Church, "Broadband Microwave Frequency Characterization of 3-D Printed Materials," *IEEE Trans. on Compon., Packag. and Manuf. Technol.*, vol. 3, pp. 2147-2155, 2013.
- [54] M. Y. Koledintseva, R. E. DuBroff, and R. W. Schwartz, "A Maxwell Garnett model for dielectric mixtures containing conducting particles at optical frequencies," *Progress In Electromagnetics Research*, vol. 63, pp. 223-242, 2006.
- [55] MatterHackers, "How to succeed when printing in PLA," [Online]. Available: <http://www.matterhackers.com/articles/how-to-succeed-when-printing-in-pla>, 2014.
- [56] Slic3r, "G-code generator for 3D printers," [Online]. Available: <http://slic3r.org/>, 2014.
- [57] Slic3r Manual, "Infill Patterns and Density," [Online]. Available: <http://manual.slic3r.org/expert-mode/infill>, 2014.

- [58] M. Y. Koledintseva, A. G. Razmadze, A. Y. Gafarov, V. V. Khilkevich, J. L. Drewniak, and T. Tsutaoka, "Attenuation in extended structures coated with thin magneto-dielectric absorber layer," *Progress In Electromagnetics Research*, vol. 118, pp. 441-459, 2011.
- [59] C. T. Dervos, Ef. Thirios, J. Novacovich, P. Vassiliou, P. Skafidas, "Permittivity properties of thermally treated TiO₂", *Materials Letters*, 58 pp. 1502 – 1507, 2004.
- [60] N. Klein, C. Zuccaro, U. Dähne, H. Schulz, N. Tellmann, R. Kutzner, A. G. Zaitsev, and R. Wördenweber, "Dielectric properties of rutile and its use in high temperature superconducting resonators", *Journal of Applied Physics*, vol. 78, no. 11, pp. 6683-6686, 1995.
- [61] W. Qian, G. Li, P. Maheshwari, C. Ding, D. White, S. Scarce, Y. Yang, V. Khilkevich, D. Pommerenke, "Emulation of Lossy Channel using a Low Loss Microstrip Trace with Added Lossy Material," *IEEE Int. Symp. Electromag. Compat.*, pp. 945-949, 2014.
- [62] A. Koul, P. Anmula, M. Koledintseva, J. Drewniak and S. Hinaga, "Improved technique for extracting parameters of low-loss dielectrics on printed circuit boards", *IEEE Int. Symp. Electromag. Compat.*, pp.191-196, 2009.
- [63] M. Y. Koledintseva, J. Xu, S. De, J. L. Drewniak, Y. He, and R. Johnson, "Systematic analysis and engineering of absorbing materials containing magnetic inclusions for EMC applications", *IEEE Trans. on Magnetics*, vol. 47, pp. 317-323, 2011.
- [64] K. O. Hill, G. Meltz, "Fiber Bragg grating technology fundamentals and overview," *Journal of Lightwave Technology*, vol. 15, no. 8, pp. 1263-1276, 1997.
- [65] 3D Printer World, "3D Printing Materials Inventor Kai Parthy," [Online]. Available: <http://www.3dprinterworld.com/article/3d-printing-materials-inventor-kai-parthy>, 2014.

VITA

Xiangyang was born in Xinji, Hebei, China. He received his B.S. and M.S. degree in Optical Engineering from Northwestern Polytechnical University, Xi'an, China, in 2009 and 2012. He joined the EMC Laboratory in the Missouri University of Science and Technology, Rolla, in 2013 and received the M.S. degree of Electronic Engineering in December 2015. He also worked as a Co-op Engineer at Cisco EMC Design Team from 2014 to 2015.

His research interests include near field scanning technology, emission source identification, 3D Printing technology on the electromagnetic applications, lossy material property, EMC and SI modeling, and high-frequency measurement.